Predicting the thioflavin fluorescence of retinal amyloid deposits in association with Alzheimer's disease and differentiating amyloid protein from alpha-syn

by

Yunyi Qiu

A thesis

presented to the University of Waterloo

in fulfillment of the

thesis requirement for the degree of

Master of Science

in

Physics (Nanotechnology)

Waterloo, Ontario, Canada, 2020

Author's Declaration

This thesis consists of material all of which I authored or co-authored: see Statement of Contributions included in the thesis. This is a true copy of the thesis, including any required final revisions, as accepted by my examiners.

I understand that my thesis may be made electronically available to the public.

Statement of Contributions

The thesis author is the sole author of all written chapters except as described below. There were coauthors for earlier material presented at conferences and for a published journal paper as well as for material within the thesis:

Coauthors for Annual Meeting of the Association for Research in Vision and Ophthalmology (ARVO 2019) on which I was the first author (*Predicting the positivity for thioflavin fluorescence of retinal deposits by their polarization properties in association with Alzheimer's disease*) are Tao Jin, Erik Mason, Rachel Redekop, Laura Emptage, Monika Kitor and Melanie CW Campbell.

Coauthors for the Journal paper published in Translational Vision Science and Technology (TVST) on which I was the first author (*Predicting thioflavin fluorescence of retinal amyloid deposits associated with Alzheimer's disease by their polarimetric properties*) (Translational Vision Science & Technology August 2020, Vol.9, 47. doi:https://doi.org/10.1167/tvst.9.2.47) are Tao Jin, Erik Mason, Melanie CW Campbell.

In Chapter 2, the paper work published in the TVST journal is presented, in which I am the first author, the person who implemented the classification models, oversampling methods and evaluation metrics, prepared and ran the corresponding code, interpreted the machine learning results and wrote the initial manuscript draft; Erik Mason created the segmentation code for segmenting deposits and the automated code for calculating the polarimetric properties; Tao Jin helped with the choices of machine learning algorithms and hyper parameters and their code implementation; Dr. Melanie CW Campbell developed the idea of using a polarimetry device for retinal amyloid detection, contributed to the design of this project, interpreted the results and edited the manuscript. Rachel Redekop, Monika Kitor and Laura Emptage prepared and imaged the simples and edited the manuscript. I acknowledged their contributions in the acknowledgement of the paper and gratefully acknowledge them again here. The Mueller matrix microscope was designed by Prof. Campbell and code for automation was by Frank Corapi and Riley Delaney.

The donated post-mortem tissue on which measurements in chapters 3 were performed, was arranged by Profs. Robin Ging-Yuek Hsiung and Ian MacKenzie of the Vancouver Coastal

Abstract

Alzheimer's disease (AD) is a neurodegenerative disease and the most common cause of dementia. According to the World Health Organization (WHO) in 2019, dementia affects around 50 million people worldwide and this number is still going to increase by 10 million every year. Currently, some treatments can delay the symptoms but no effective cure is available for AD. Part of the reason is that the current definitive diagnosis of AD can only occur after patients' death, by finding two hallmarks, amyloid-β (Aβ) plaques and tau proteins, in patients' brains. Although the early confirmation of amyloid in the brain can be achieved by using positron emission tomography (PET) or analyzing cerebral spinal fluid (CSF), both of them are invasive to human health, PET also involves expensive procedures.

Fortunately, the over-accumulation of one hallmark Aβ has also been found in the retinas of AD patients, which Dr. Campbell's group has shown is naturally birefringent under polarized light. Considering the optical accessibility of the retina, our group has proposed that polarimetry imaging device could be a strong candidate as an early diagnostic method for AD. The presumed retinal amyloid deposits have been detected by our Mueller matrix polarimetry method *ex vivo*. Since thioflavin fluorescence is a biomarker for amyloid, we stained the retinal deposits with thioflavin dye and then imaged using fluorescence microscopy to determine the existence of a thioflavin fluorescence signal. To avoid the use of a dye in future *in vivo* live eye imaging, this thesis presents a method to predict the existence of thioflavin fluorescence of retinal deposits from their interactions with polarized light by combining polarimetry and machine learning. Three machine learning algorithms have been trained and tested, two oversampling methods have been applied to solve the problem of the low number of non-fluorescence deposits as polarimetry detects amyloid with high accuracy. The results suggest that the fluorescent retinal deposits can be differentiated from non-fluorescence deposits with high accuracy, and two polarimetric properties appear have high importance in predicting thioflavin fluorescence.

To ensure that the source of fluorescence is amyloid-β protein, the second research project in this thesis aims to differentiate pure amyloid-β protein deposits from another protein alpha-synuclein, which contains a β-sheet structure and amyloid-like fibrils thus also show positivity in thioflavin fluorescence. A powerful convolutional neural network model (CNN) -the residual neural network, also known as Resnet, has been applied to differentiate the polarization images of pure

Aβ-42 protein deposits, which is the amyloid that most relevant for AD, from the alpha-synuclein pure protein. The performance of CNNs trained by images of different polarimetric properties is compared with the machine learning algorithm used before. The CNN models, which directly take the images of the polarimetric properties as input, have outperformed the machine learning algorithms tested in differentiating Aβ-42 and alpha-synuclein protein deposits. The results reported here may be useful to assist in the label-free detection of these two types of retinal amyloid deposits in live-eye imaging.

Acknowledgments

I would like to first thank my parents for supporting me to study abroad, both mentally and financially. I would like to thank my group members who have always offered me tremendous help, to Tao Jin (Harry), Erik Mason, Peter Neathway, Steven Kenneth, Julia Zangoulos who shared their code and discussed technique problems with me, to Laura Emptage, Rachel Redekop, Monika Kitor for imaging the retinas the data from which I used, to Rachel Redekop and Monika for proofreading my paper and thesis.

I also like to thank my friends Kun Zu, Xin Sun, Xuchu Yuan, Ji Ren, Lihong and Ying, who have offered me generous support during my three years studying abroad.

Lastly, I wish to thank my supervisor Dr. Melanie Campbell for her supervision, guidance and most importantly, her trust in my research. She is the person who gives me the utmost support.

Dedication

Dedicated to my parents and my friends

Contents

List of Figures

List of Tables

List of Abbreviations

AD   Alzheimer's disease

PD   Parkinson's disease

FTLD   Frontotemporal lobar degeneration

CAA   Cerebral amyloid angiopathy

Aβ   Amyloid beta

Alpha-syn Alpha-synuclein

ATN   Amyloid, tau and neurodegeneration

CSF   Cerebral spinal fluid

PET   Positron emission tomography

MRI   Magnetic resonance imaging

PSG   Polarization state generator

PSA   Polarization state analyzer

QWP   Quarter wave plate

LDA   Linear discriminant analysis

SVM   Support vector machine

RF   Random forest

t-SNE   t-distributed stochastic neighbor embedding

CNN   Convolutional neural network

Resnet   Residual network

STD   Standard deviation

ACC   Accuracy

SEN   Sensitivity

SPE   Specificity

LR   Linear retardance

LA   Linear anisotropy

LD   Linear diattenuation

ReLU   Rectified Linear Unit

SGD   Stochastic gradient descent

ROC   Receiver operating characteristic

AUC   Area under the receiver operating characteristic curve

ILSVRC ImageNet Large Scale Visual Recognition Challenge

Chapter 1

1 Introduction

1.1 Introduction of Alzheimer's disease

Alzheimer's disease (AD) is the most common cause of dementia which gives rise to the cognitive difficulties for patients and, in its late stages leads to death. It is currently the 6th leading cause of death in the United States[1]. Currently, AD is usually only definitely diagnosed after death, by characterizing the over-accumulation of the insoluble plaques composed of the amyloid-beta (Aβ) protein inside the brain[2]. Before death, positron emission tomography (PET) amyloid or tau brain scans are also used in trials of therapies for AD or in some jurisdictions, (for example, the Canadian province of Quebec), they are funded for use when a diagnosis is difficult. PET brain scans and another early diagnostic method (analyzing proteins in cerebral spinal fluid (CSF)) are invasive and very expensive. For example, per PET scan costs 900 to 1400 USD[3] and very few hospitals have the scanners.

However, an over-accumulation of Aβ has also been found in the retina of those with AD. and Dr. Campbell's lab has shown that the Aβ is naturally birefringent under polarized light[4]. Thus, a non-invasive, inexpensive method using polarimetry has been proposed by our group for the label-free detection of the amyloid deposits and the early onset of AD[4]. The two research projects introduced in this thesis combine polarimetry with machine learning and a deep neural network, with the aim of replacing staining of the deposits in *in vivo* live eye imaging for AD early diagnosis which is invasive.

Further information on AD and AD diagnosis can be found in section 2.1.

1.2 Polarized light, Stokes vector and Mueller matrix

In this project, polarized light is used to interact with the samples, the Stokes vector is used to describe the polarization state of the light and the Mueller matrix is used to measure the change of the polarization state during interaction with the tissue. The polarized light, Stokes vector and Mueller matrix are introduced in the following.

Light can be described as an electromagnetic wave, which has electric field component E and magnetic field component, B perpendicular to the propagation of light. Because of this, light as a plane wave tends to exhibit the property called polarization. The polarization is defined here as the direction of the electric field vibration relative to the direction of light propagation. Imaging a plane wave propagating in the z-direction, its electric field components in the x-direction $E_x(z,t)$ and y-direction $E_y(z,t)$ can be written as

$$E_x(z,t) = A_X(t)\cos(\tau + \delta_x) \tag{1.1}$$

$$E_y(z,t) = A_y(t)\cos(\tau + \delta_y) \tag{1.2}$$

where $A_X(t)$ and $A_y(t)$ are the wave amplitudes in the x and y directions, δ_x and δ_y are the phases in these two directions. $\tau = \omega t - kz$ is the propagator term, where ω and k are the angular frequency and wavenumber of this light wave propagating in the z-direction.

Now, we can rearrange Eqs 1.1 and 1.2 to display the locus of the endpoint of the electric field as it propagates through a period, by first dividing the amplitudes,

$$\frac{E_x(t)}{A_x(t)} = \cos(\tau)\cos(\delta_x) - \sin(\tau)\sin(\delta_x) \tag{1.3}$$

$$\frac{E_y(t)}{A_y(t)} = \cos(\tau)\cos(\delta_y) - \sin(\tau)\sin(\delta_y) \tag{1.4}$$

then by combining the phase terms δ_x and δ_y, this gives,

$$\frac{E_x(t)}{A_x(t)}\sin(\delta_y) - \frac{E_y(t)}{A_y(t)}\sin(\delta_x) = \cos(\tau)\sin(\delta_y - \delta_x) \tag{1.5}$$

$$\frac{E_x(t)}{A_x(t)}\cos(\delta_y) - \frac{E_y(t)}{A_y(t)}\cos(\delta_x) = \sin(\tau)\sin(\delta_y - \delta_x) \tag{1.6}$$

and finally by squaring and adding Eq 1.5 and Eq 1.6, one gets

2

$$\frac{E_x(t)^2}{A_x(t)^2} + \frac{E_y(t)^2}{A_y(t)^2} - 2\frac{E_x(t)\,E_y(t)}{A_x(t)\,A_y(t)}\cos(\delta) = sin^2(\delta) \qquad (1.7)$$

where $\delta = \delta_y - \delta_x$. It is clear that Eq 1.7 describes a trajectory in an ellipse shown in Fig 1.1, known as the polarization ellipse.
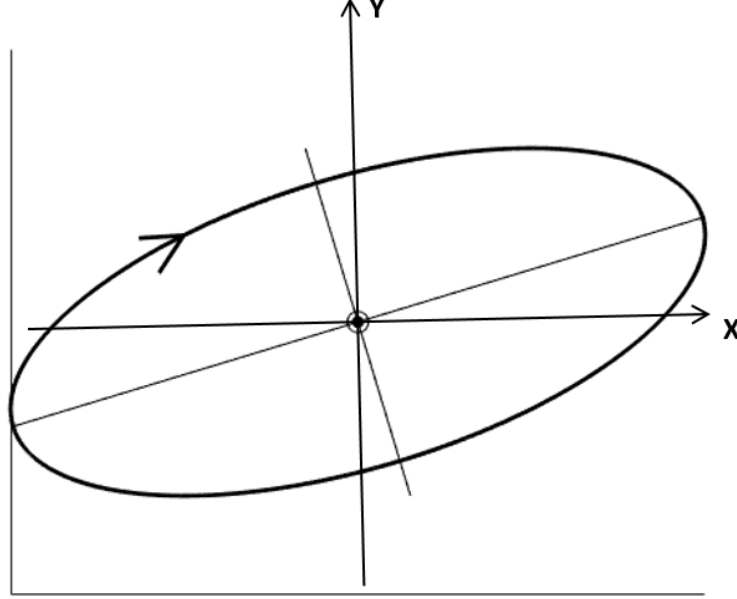
Figure 1.1 The schematic of the polarization ellipse.

Multiplying Eq 1.7 by $4A_x(t)^2 A_y(t)^2$ and taking time averages represented by $\langle\,...\,\rangle$ gives

$$4\langle A_y(t)^2 E_x(t)^2\rangle + 4\langle A_x(t)^2 E_y(t)^2\rangle - 8\langle A_x(t)A_y(t)E_x(t)E_y(t)\cos(\delta)\rangle = 4\langle (A_x(t)A_y(t)sin(\delta))^2\rangle (1.8)$$

For monochromatic waves, the amplitudes are constant, and the time average of $E_i(t)$ and $E_j(t)$ can be computed using $\langle E_i(t)E_j(t)\rangle = \lim_{T\to\infty}\frac{1}{T}\int_0^T E_i(t)E_j(t)dt$. So Eq 1.8 can be written as

$$4A_x{}^2 A_y{}^2 - 4\big(A_xA_y\cos(\delta)\big)^2 = \big(A_xA_y\sin(\delta)\big)^2 \qquad (1.9)$$

which is equivalent to,

$$\big(A_x{}^2 + A_y{}^2\big)^2 - \big(A_x{}^2 - A_y{}^2\big)^2 - (2A_xA_y cos(\delta))^2 - (2A_xA_y sin(\delta))^2 = 0 \qquad (1.10)$$

3

From here, we define the Stokes vector (S_0, S_1, S_2, S_3) as

$$\begin{pmatrix} S_0 = A_x{}^2 + A_y{}^2 \\ S_1 = A_x{}^2 - A_y{}^2 \\ S_2 = 2A_x A_y cos(\delta) \\ S_3 = 2A_x A_y sin(\delta) \end{pmatrix} \tag{1.11}$$

Obviously, $S_0{}^2 = S_1{}^2 + S_2{}^2 + S_3{}^2$. where S_1, S_2 and S_3 represent the intensity differences in the horizontal and vertical linear polarizations, +45° and -45° linear polarizations, and right and left circularly polarized light, respectively.

When a beam of polarized light with Stokes vector **S** interacts with a media, its polarization state will change into a new one $\boldsymbol{S}' = \{S_0', S_1', S_2', S_3'\}$, where

$$\begin{pmatrix} S_0' = m_{00}S_0 + m_{01}S_1 + m_{02}S_2 + m_{03}S_3 \\ S_1' = m_{10}S_0 + m_{11}S_1 + m_{12}S_2 + m_{13}S_3 \\ S_2' = m_{20}S_0 + m_{21}S_1 + m_{22}S_2 + m_{23}S_3 \\ S_3' = m_{30}S_0 + m_{31}S_1 + m_{32}S_2 + m_{33}S_3 \end{pmatrix} \tag{1.12}$$

The above linear relationship can be written in the matrix form:

$$\begin{Bmatrix} S_0' \\ S_1' \\ S_2' \\ S_3' \end{Bmatrix} = \begin{pmatrix} m_{00} & m_{01} & m_{02} & m_{03} \\ m_{10} & m_{11} & m_{12} & m_{13} \\ m_{20} & m_{21} & m_{22} & m_{23} \\ m_{30} & m_{31} & m_{32} & m_{33} \end{pmatrix} \begin{Bmatrix} S_0 \\ S_1 \\ S_2 \\ S_3 \end{Bmatrix} \tag{1.13}$$

$$\mathbf{M} = \begin{pmatrix} m_{00} & m_{01} & m_{02} & m_{03} \\ m_{10} & m_{11} & m_{12} & m_{13} \\ m_{20} & m_{21} & m_{22} & m_{23} \\ m_{30} & m_{31} & m_{32} & m_{33} \end{pmatrix} \tag{1.14}$$

The 4-by-4 matrix **M** written here is called the Mueller matrix, it describes quantitatively the change of the state of the polarized light during the interaction. The polarimetric properties used in experimental Chapters 2 and 3 can each be computed from the Mueller matrix, from the equations listed in the Appendix 2.

1.3 Polarimetry and polarimetric properties

To measure the Mueller matrix of a sample, transmission Mueller matrix polarimetry is used which is composed of a polarization state generator (PSG) and a polarization state analyzer (PSA). A diagram of polarimeter was shown in Fig 2.1, Chapter 2. Our polarimetry measurements are taken in a Nikon transmission microscope, retrofitted with a 633nm filter to produce red incoherent light. The PSG consists of a horizontal polarizer M_p followed by a quarter wave plate (QWP) with its fast axis at an angle θ, relative to the linear polarizer, giving M_{qwp}. The QWP is followed by a linear polarizer in the PSA. The Mueller matrix of the linear polarizer is:

$$M_p = \frac{1}{2} \begin{pmatrix} 1 & 1 & 0 & 0 \\ 1 & 1 & 0 & 0 \\ 0 & 0 & 0 & 0 \\ 0 & 0 & 0 & 0 \end{pmatrix} \tag{1.15}$$

And, as the QWP fast axis is rotated to an angle, θ relative to the axis of the polarizer,

$$M_{qwp} = \begin{pmatrix} 1 & 0 & 0 & 0 \\ 1 & cos^2(2\theta) & \cos(2\theta)\sin(2\theta) & -\sin(2\theta) \\ 0 & \cos(2\theta)\sin(2\theta) & sin^2(2\theta) & \sin(2\theta) \\ 0 & \sin(2\theta) & -\cos(2\theta) & 0 \end{pmatrix} \tag{1.16}$$

Thus, for a beam of unpolarized input light $S_{in} = (1,0,0,0)^T$, after going through the PSG, it will have a new polarization state $S_G(\theta_g)$, where θ_g is the angle of the fast axis for the QWP in the PSG.

$$S_G(\theta_g) = \frac{1}{2}\left(1, cos^2(2\theta_g), \cos(2\theta_g)\sin(2\theta_g), \sin(2\theta_g)\right)^T \tag{1.17}$$

Note that the output light $S_G(\theta_g)$ has become polarized with an intensity, $S_0 = 1$, such that $S_0{}^2 = S_1{}^2 + S_2{}^2 + S_3{}^2$.

The light will then interact with the sample Muller matrix M_s, and go through the PSA. The output S' can be expressed as

$$S' = M_{PSA}M_sM_{PSG}S_{in} \tag{1.18}$$

Where M_{PSA} and M_{PSG} represent the Muller matrix of the PSA and PSG, respectively and M_s is the Mueller matrix of the sample being measured.

Since only the beam intensity of S' can be measured, to solve for the elements in the 4×4 Muller matrix, a 4×4 intensity matrix I can be constructed by rotating the QWPs in the PSG and PSA to 4 different angles, respectively.

$$\begin{pmatrix} I_{G1}I_{A1} & I_{G2}I_{A1} & I_{G3}I_{A1} & I_{G4}I_{A1} \\ I_{G1}I_{A2} & I_{G2}I_{A2} & I_{G3}I_{A2} & I_{G4}I_{A2} \\ I_{G1}I_{A3} & I_{G2}I_{A3} & I_{G3}I_{A3} & I_{G4}I_{A3} \\ I_{G1}I_{A4} & I_{G2}I_{A4} & I_{G3}I_{A4} & I_{G4}I_{A4} \end{pmatrix} = M_{PSA}M_sM_{PSG} \tag{1.19}$$

Where $I_{Gm}I_{An}$ represents the intensity exiting the instrument when the PSG is at angle, θ_m and PSA is at angle θ_n.

Thus, by inverting the matrix M_{PSA} and M_{PSG}, the elements in the Mueller matrix of the material being measured can be calculated as

$$M_s = (M_{PSA})^{-1}I(M_{PSG})^{-1} \tag{1.20}$$

The resulting image will be a spatially-resolved Mueller matrix image, which means the Mueller matrix of the sample will be calculated at each pixel of the original measurements.

As mentioned earlier in Section 1.2, the polarimetric metrics listed in the Appendix can each be calculated from the Mueller matrix, M_s. When measuring amyloid deposits in retinal tissue in Chapter 2, two metrics, linear anisotropy (LA) and linear retardance (also known as retardation) (LR), show high importance. LR is the linear component of the retardance, which describes the resultant relative phase difference between two orthogonal polarization components after they traverse the retinal sample. Our group has also found that LR gives the highest contrast between the amyloid deposits and the surrounding retina background. The retardance we detected in turn must result from the birefringent nature of the retinal deposits, which is a different refractive index is seen by the two orthogonal polarizations of the light. Although amyloid deposits stained with the dye Congo red are known to be birefringent[5], our group is the first to demonstrate intrinsic birefringence in unstained deposits[6]. Retardance of the sample can be derived using the retarder matrix M_R from the polar decomposition of the measured matrix[7] $M = M_\Delta M_R M_D$, where M_R is in the form of

$$M_R = \begin{pmatrix} 1 & 0^T \\ 0 & m_R \end{pmatrix} \tag{1.21}$$

The m_R is a 3-by-3 matrix, and the retardance vector can be calculated by

$$\vec{R} = \cos^{-1}\left[\frac{tr(M_R)}{2} - 1\right] \tag{1.22}$$

The first two components of $\vec{R}$ are linear (horizontal/ vertical, and 45°/ -45°), the third is circular retardance.

LA is a quantitative measurement of the polarimetric anisotropy caused by the linear components of retardance and diattenuation which are relative to the horizontal axis. To derive LA, one can present the Mueller matrix in the form of

$$\text{M} = m_{00} \begin{pmatrix} 1 & D_1 & D_2 & D_3 \\ P_1 & k_1 & r_3 & -r_2 \\ P_2 & q_3 & k_2 & r_1 \\ P_3 & -q_2 & q_1 & k_3 \end{pmatrix} \tag{1.23}$$

The anisotropies between symmetric elements in the Mueller matrix are then defined as follow:

$$\begin{aligned}
\alpha_{1D} &\equiv D_1 + P_1, \ \alpha_{1R} \equiv r_1 - q_1 \\
\alpha_{2D} &\equiv D_2 + P_2, \ \alpha_{2R} \equiv r_2 - q_2 \\
\alpha_{3D} &\equiv D_3 + P_3, \ \alpha_{3R} \equiv r_3 - q_3
\end{aligned} \tag{1.24}$$

Where α_{1D}, α_{1R} refer to the linear horizontal anisotropy from diattenuation and retardance; α_{2D}, α_{2R} correspond to the linear 45° anisotropy, α_{3D}, α_{3R} correspond to circular anisotropy.

Thus, the anisotropy coefficients of linear horizontal, linear 45° and circular components can be defined as

$$\alpha_1 \equiv \sqrt{\frac{\alpha_{1D}{}^2 + \alpha_{1R}{}^2}{\Sigma}}$$

$$\alpha_2 \equiv \sqrt{\frac{\alpha_{2D}{}^2 + \alpha_{2R}{}^2}{\Sigma}} \tag{1.25}$$

$$\alpha_3 \equiv \sqrt{\frac{\alpha_{3D}{}^2 + \alpha_{3R}{}^2}{\Sigma}}$$

Σ can be interpreted as the description of total polarimetric anisotropy, defined as

$$\Sigma \equiv 3 - k^2 + 2D^T P - 2r^T q \tag{1.25}$$

Where $D \equiv \begin{pmatrix} D_1 \\ D_2 \\ D_3 \end{pmatrix}$, $P \equiv \begin{pmatrix} P_1 \\ P_2 \\ P_3 \end{pmatrix}$, $k \equiv \begin{pmatrix} k_1 \\ k_2 \\ k_3 \end{pmatrix}$, $r \equiv \begin{pmatrix} r_1 \\ r_2 \\ r_3 \end{pmatrix}$, $q \equiv \begin{pmatrix} q_1 \\ q_2 \\ q_3 \end{pmatrix}$ for simplicity.

Thus, the value of $LA = \sqrt{\alpha_1^2 + \alpha_2^2}$, and circular anisotropy equals α_3.

Linear diattenuation (LD) is another important metric we used in the analysis of Chapter 3. LD is the linear component of diattenuation, which describes the dependency of light transmittance on its polarization state (the light with different polarization states will be absorbed by different amounts). Diattenuation can be derived from the 4×4 Mueller matrix introduced before, which can also be written as

$$M = m_{00} \begin{pmatrix} 1 & D^T \\ P & m \end{pmatrix} \tag{1.26}$$

where $D^T = (m_{01}, m_{02}, m_{03})$ is called the diattenuation vector. m_{01}, m_{02} are the horizontal/vertical and 45°/ -45° diattenuation values which combine to give linear diattenuation. So the value of LD is

$$LD = \sqrt{m_{01}^2 + m_{02}^2} \tag{1.27}$$

1.4 Fluorescence microscope

In this research, the fluorescence microscope was used to examine the thioflavin fluorescence of sample deposits. Samples need to be stained with Thioflavin-S and counterstained with DAPI before being viewed with the microscope. The fluorescence microscope takes the light reflected from the sample, the excitation wavelength for fluorescence microscope is in the wavelength of blue light (490nm), with emission in green wavelength (525nm).

1.5 Theory of Neural Networks

Research on neural networks has been ongoing since the 1940s, and its definition now varies in different disciplines. This thesis takes the concept proposed by Kohonen, which defines the neural networks as "massively parallel interconnected networks of simple adaptive elements and their hierarchical organizations which are intended to interact with the objects of the real world in the same way as biological nervous systems do"[8].

The "simple adaptive elements" refers to the basic computational unit "neuron" in the network, which is a mathematical model of the real neuron in the brain proposed by McCulloch and Pitts[9]. As shown in Fig 1.2, the current neuron (the yellow circle) is getting input signals from other neurons (represented by x_i for the ith neuron), which travel through the connections and interact multiplicatively with weighting (w_i for the ith connection). A bias term (b) is added to the weighted sum ($\sum_i w_i x_i$) which functions as the intercept in a linear equation to help the neuron model better fit the given input.
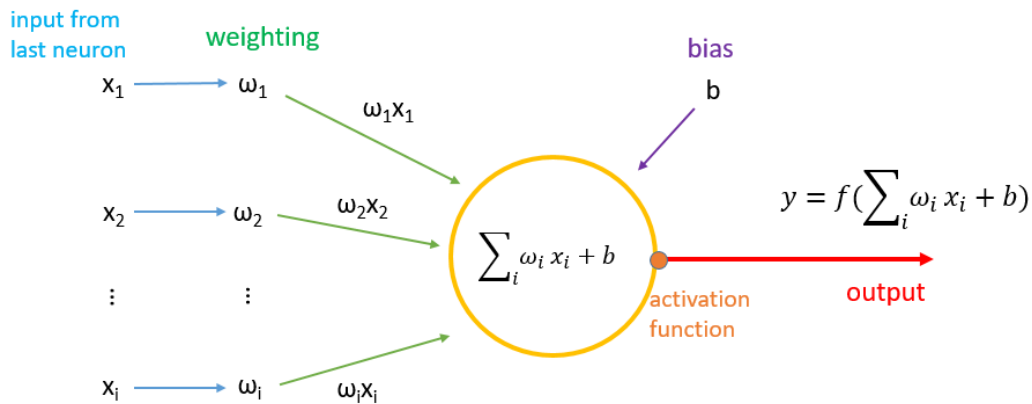
Figure 1.2. The schematic of the neuron model proposed by McCulloch and Pitts.

The weighted sum with bias ($\sum_i \omega_i x_i + b$) finally yields the output of the current neuron by applying an activation function. In this project, the Rectified Linear Unit (ReLU)[10] is used as the activation function. The formula of ReLU is given by,

$$f(x) = \max(0, x) \tag{1.28}$$

The neurons can be "parallel interconnected" to become a network known as a fully-connected network[11], shown in Fig 1.3. The external input is taken by the neurons in the input layer, the signal is processed in the hidden layers and output layer, and the final output is coming from the neurons in the output layer.

Input layer   Hidden layers   Output layer
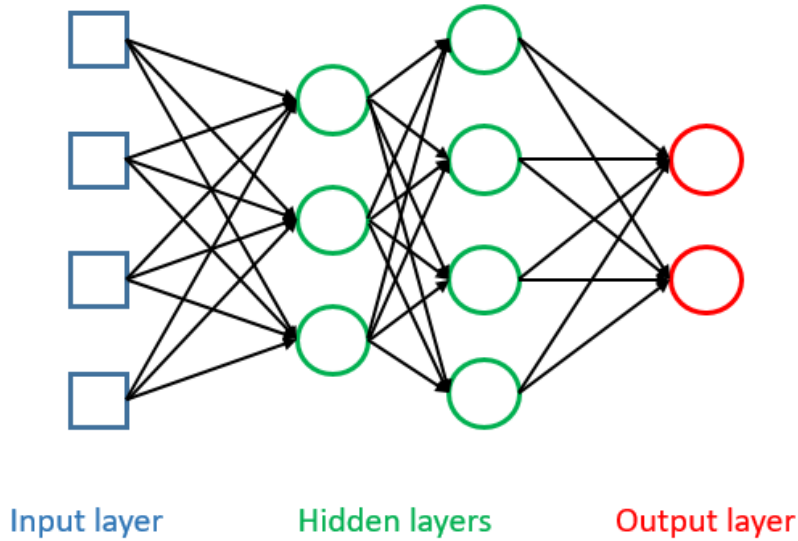
Figure 1.3. The schematic of a fully connected neural network

The process of learning for a network is the process of updating the connection weights between each neuron. One can compare the output from the network with the real label of the input and update the weight by following a certain learning rule. In this research, the backpropagation algorithm[12] based on stochastic gradient descent (SGD) strategies[13] was applied to train the neural network. The algorithm first measures the error of the output to the label E_k, then tracks the error in reverse by computing the error gradient across all connection weights, and finally updates the weight by gradient descent. The detailed calculation is as follows.

$$E_k = L(y, y_k) \tag{1.29}$$

where y is the real label and y_k is the output from the network, L is the loss function. For a binary classification, the label y can be set to {0, 1}; for a multiclass classification, for example three classes, the label y can be represented in the form of {[1,0,0], [0,1,0], [0,0,1]}. In this research, we use cross entropy loss, given by

$$L(y, y_k) = -[y\log(y_k) + (1 - y)\log(1 - y_k)] \qquad (1.30)$$

Thus, one can minimize $L(y, y_k)$ with respect to y_k to get the prediction y_k closer to the real label y. For example, if y_k = y = 0 or y_k = y =1, $L(y, y_k)$ will be zero.

For a given learning rate η, one can get,

$$\Delta w_{hj} = -\eta \frac{\partial E_k}{\partial w_{hj}} \qquad (1.31)$$

where Δw_{hj} is the update for the connection weight between the hth neuron and the jth.

Notice that w_{hj} first determines the output from the hth neuron β_j, then affects the output from the jth neuron y_k, and finally affects E_k.

$$\frac{\partial E_k}{\partial w_{hj}} = \frac{\partial E_k}{\partial y_k} \frac{\partial y_k}{\partial \beta_j} \frac{\partial \beta_j}{\partial w_{hj}} \qquad (1.32)$$

Thus, the updated connection weight between the hth and jth neurons will be,

$$w'_{hj} = w_{hj} - \eta \frac{\partial E_k}{\partial w_{hj}} \qquad (1.33)$$

1.6 Theory of Convolutional Neural Networks

When David H Hubel and Torsten Wiesel studied the visual cortex of cats in the 1950s, they found that some neurons in the visual cortex have a small local receptive field and can only recognize some simple shapes such as a horizontal or a vertical lines[14,15]. However, they can pass these simple shapes to the higher-level neurons which have larger local receptive fields, allowing the visual system of the cats to detect more complex patterns[14,15]. This result inspired the research in the field of neural networks and computer vision and later the concept of "convolutional neural network (CNN)" was proposed. In 1998, Yann LeCun *et al.* proposed the famous CNN architecture – LeNet-5[16]. This fundamental network is the origin of many modern CNN architectures and it introduces two new building blocks of CNN that are not included in the concept of neural network – convolutional layers and pooling layers.

1.6.1 Convolutional layers

A neuron in the convolutional layers has a small receptive field. Unlike in a fully connected layer, they are not connected to every single pixel/neuron in the previous layer. For example, the neurons in the first convolutional layer are only connected to some pixels of the input image within their receptive fields, and only those neurons (first convolutional layer) in the receptive fields of the second convolutional layer are connected to the corresponding neuron in the second convolutional layer. This allows the subsequent convolutional layer to extract higher-level features based on the output of the previous layer, while the previous convolutional layer can focus on more fundamental features. A schematic of this convolution is shown in Fig 1.4.
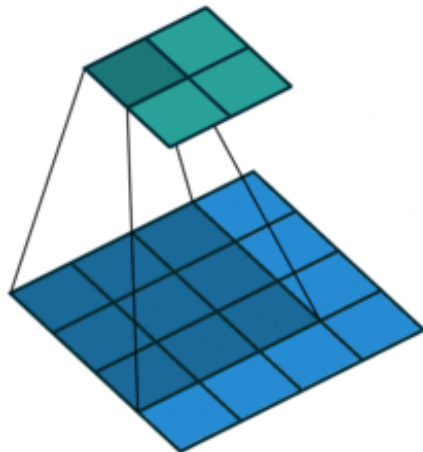
Figure 1.4. Convolution between layers with no padding and stride = 1, included with the permission of the author in Appendix 3 [17]. The blue map is the input layer, the cyan map is the output layer. The dark blue square is the receptive field of the neuron in the cyan map.

The weights of the neurons in the receptive field are called the filter. The weights will change during training, so CNN can find the most useful filter according to its task. The length of the receptive field is called the filter size, which equals three in the example in Fig 1.4. In addition to filter size, other spatial parameters that determine the size of the output are the depth of the filter, stride and zero-padding. One can stack multiple filters to get a 3D filter, the depth of which

equals to the number of the included filters. The stride is the spacing when we slide the filter in the plane of the receptive field. In the example of Fig 1.4, the filter is moved one pixel at a time, so the stride is equal to 1. Finally, in order to get a specific output size, it is common to pad zeros around the inputs, which is called zero-padding. Fig 1.5 displays a sample convolution with zero-padding and a different stride, both set to 2.
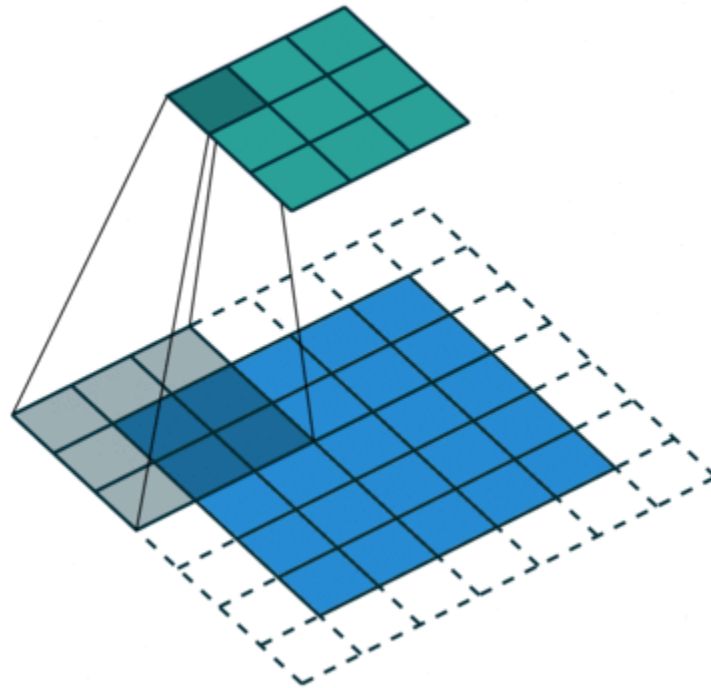
Figure 1.5. Convolution between layers with zero padding = 2 and stride = 2, included with the permission of the author in Appendix 3 [17]. The blue map is the input layer, the cyan map is the output layer. The dark blue square is the receptive field of the neuron in the cyan map. The white region is zero-padding.

In Fig 1.5, both the width and height of the input layer are increased by 2 due to zero-padding, so the value of zero-padding is 2. The filter moves 2 pixels at a time, which means the stride equals 2 as well. Generally, for an input with the size $W_1 \times H_1 \times D_1$ (where W, H and D are width, height and depth), if the filter has the size equal to F with a stride S and zero-padding P, the size of the output will be,

$$W_2 = \frac{W_1 - F + 2P}{S} + 1 \qquad (1.34)$$

$$H_2 = \frac{H_1 - F + 2P}{S} + 1 \qquad (1.35)$$

1.6.2 Pooling layers

The principle of pooling layers is similar to convolutional layers. The neurons in the pooling layer are also only connected to the neurons in the previous layer within the corresponding receptive field. The size of the field, stride and zero-padding need to be specified in the same way as for the convolutional layer. The only difference is that there are no weights in the pooling layer, instead, the output size is reduced by simply taking the average or the maximum of the receptive field. In this project, Max-pooling is used, as shown in Fig 1.6.
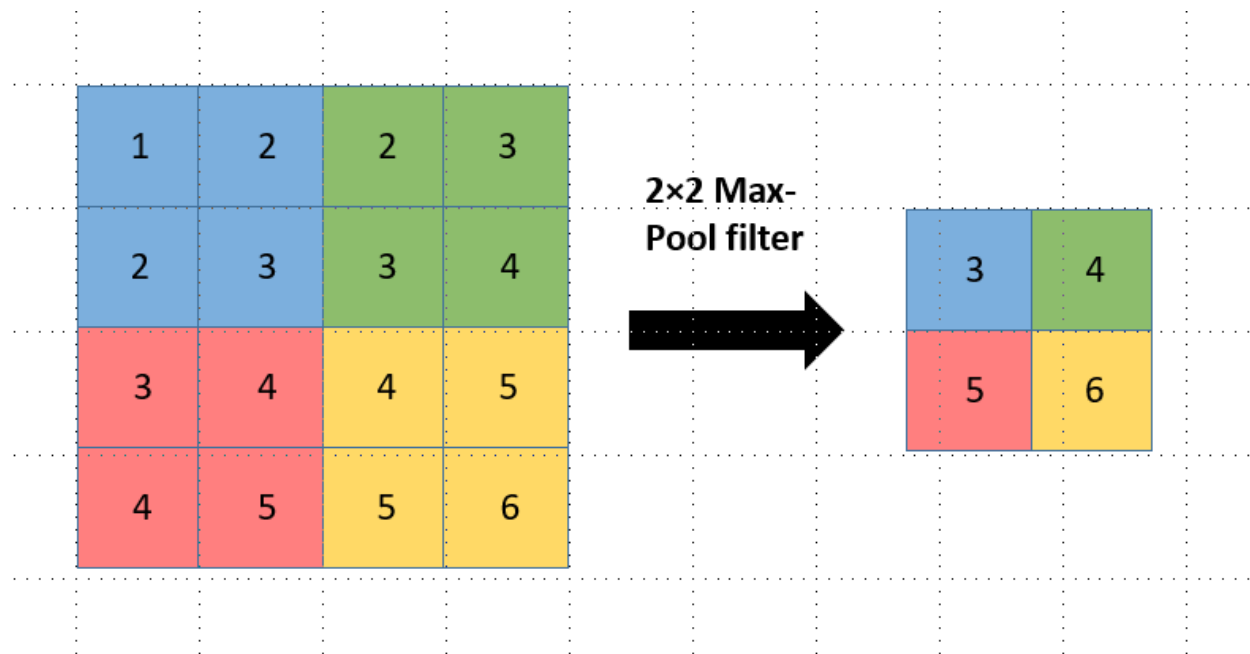
Figure 1.6. A schematic of max-pooling. The 4×4 matrix represents the input, after max-pooling, the output is a 2×2 matrix.

In Fig 1.6, the size of the Max-pool filter is 2, the stride is 2, which perfectly fits the 4×4 input matrix to generate a 2×2 output, so there is no need for zero-padding. The numbers in the output are the largest in the areas of the same color as the input.

By applying pooling, computational load and memory usage can be reduced. At the same time, pooling can also slow down the overfitting due to the reduction of the number of parameters in the network.

Chapter 2

2 Predicting thioflavin fluorescence of retinal amyloid deposits associated with Alzheimer's disease by their polarimetric properties[18]

2.1 Introduction

Alzheimer's disease (AD) is a neurodegenerative disease which leads to cognitive impairment and ultimately, death. AD is the primary cause of dementia. In 2010, the worldwide prevalence of dementia was 35.6 million and this number is predicted to triple by 2050[8]. Currently, this disease can only be definitively diagnosed post-mortem through the severity of two hallmarks: amyloid plaques (composed of misfolded amyloid-β protein) and neurofibrillary tangles (composed of tau protein), both of which begin to accumulate in the brain prior to symptoms of cognitive impairment[19]. Detection of amyloid, tau and neurodegeneration (ATN) in the brain is recommended for detecting changes associated with the AD disease process in clinical trials of novel treatments[20]. Confirmation of amyloid in the brain is currently achieved using positron emission tomography (PET)[21] or analyzing cerebral spinal fluid (CSF)[22]. However, both methods are invasive: PET uses a radiative isotope injection[21], while a CSF test requires extraction of fluid from the patient's spine[22]. Currently, there is no effective cure for AD. However, it has been suggested that earlier detection of brain amyloid in prodromal disease could enable more successful treatment before damage from amyloid and tau accummulates[23]. Furthermore, the ATN framework allows for the incorporation of other biomarkers of amyloid in the brain[5]. Therefore, it is important to develop a non-invasive method to detect amyloid in association with AD prior to AD diagnosis. Potential peripheral biomarkers of AD include detection of amyloid in the retina[24].

Many changes have been measured in the retina in association with AD[25]. An over-accumulation of amyloid deposits has been found in the retinas of AD patients by our group (M.C.W. Campbell,

16

et al. IOVS 2010;51:ARVO E-Abstract 5778) and others[23,26], including immunohistochemistry positivity for the presence of amyloid-β[2,27,28] (Yuchun Tsai, et al. IOVS 2014;55:ARVO E-abstract 523-524). We demonstrated that it is possible to detect amyloid deposits in the retina using polarized light in an imaging device with animal models (Michael Tokiyoshi Hamel, *et al.* IOVS 2016;57:ARVO E-Abstract 2216) and humans (Tao Jin, *et al.* IOVS 2017;58:ARVO E-Abstract 3367; David DeVries, *et al.* IOVS 2015;56:ARVO E-Abstract 2385), as the interactions of the deposits with polarized light is significantly different from those of the surrounding retina. Retinal deposits were confirmed to be amyloid via Thioflavin-S staining[29]. Koronyo *et al.* have also demonstrated the feasibility of *in vivo* detection of retinal amyloid deposits using curcumin staining[30]. This method, however, requires the ingestion of curcumin for 2-10 days to bind with the deposits[30]. Our group has also shown that the number of amyloid deposits in the anterior retina predicts the severity of AD pathology in the brain, including severity of brain amyloid[31] (Frank Corapi, *et al*. IOVS 2018;59:ARVO E-Abstract 1582) .

Thioflavin is a fluorescent marker of amyloid, including amyloid-β, known to occur in AD. Thioflavin also stains other amyloids[32], some of which are associated with other neurodegenerative diseases[33]. In the ATN diagnostic framework for AD, amyloid PET scans are an approved method of measuring brain amyloid[20]. Similarly, a dye used in amyloid PET scans, Pittsburgh compound B, is an uncharged analog derived from thioflavin and thus marks amyloid and may not be specific to amyloid-β[34].

A number of studies have applied machine learning techniques to AD diagnosis. Two studies used a supporting vector machine (SVM) algorithm to distinguish those with AD from controls using neuroimaging data from magnetic resonance imaging (MRI)[35,36]. Another used random forest (RF) analysis on MRI data to separate those with AD from healthy controls and compared the performance of RF with SVM[37]. In optical coherence tomography, a SVM-based 3D segmentation of retinal layers has been reported in both diseased and normal retina[38]. In addition, images taken with polarized light of morphologically similar algae have been classified with a convolutional neural network[39].

In those with brain amyloid, imaging with polarized light (polarimetry) detects the majority of the deposits stained with Thioflavin-S (true positives), some deposits that are not stained by Thioflavin-S (false positives) and fails to detect a few Thioflavin-S positive deposits (false

negatives). The purpose of this study was to differentiate Thioflavin-S positive amyloid deposits (true positives) from those deposits without Thioflavin-S fluorescence (false positives), based on the polarimetric images of the deposits in order to identify amyloid deposits without the use of dye. To this end, we implemented and compared machine learning approaches which can predict the presence of retinal amyloid fluorescence using only the information from images obtained with polarized light.

2.2 Method

2.2.1 Sample preparation

2.2.1.1

Eyes (N=28) were obtained post-mortem from donors in compliance with the Declaration of Helsinki. Informed consent was obtained from the donors by our collaborators Robin Ging-Yuek Hsiung and Ian MacKenzie at UBC and the research was approved by the Human Research Ethics Committee of the University of Waterloo. Upon post-mortem examination (NIA-AA guidelines[19]) by Dr Veronica Hirsch-Reinshagen of the Vancouver General Hospital, 23 donors had a high cumulative score of AD neuropathologic change, 4 had a moderate score and 1 had a low score; all had evidence of brain amyloid. Preparation, and imaging as described herein was performed by Rachel Redekop, Monika Kitor and Laura Emptage. Eyes were immersed in 10% formalin prior to dissecting, staining and flat-mounting the retina. Retinas were stained with 0.1% Thioflavin-S, counterstained with DAPI and cover-slipped. Each retina was imaged with fluorescence and polarimetric microscopy to determine presumed amyloid deposits. In total, 920 polarization positive retinal deposits found in anterior retinal layers from 28 individuals were analyzed, including 789 deposits with fluorescence signals and 131 deposits without fluorescence signals. An additional 16 deposits had only fluorescent signals; 13 of these deposits had no polarimetric signals and 3 had unclear polarimetric signals.

2.2.1.2 Pure amyloid samples

Aβ (1-42) was purchased from rPeptide. 1 mL of 10 mM HEPES and 150 mM NaCl (pH of 7.4) was added to 0.5 mg of Aβ (1-42) and incubated at 37°C for 72 hours without shaking. Stained Aβ was prepared by adding 500 µL of filtered 1.25 mM Thioflavin-T in 50 mM of PBS and allowing

it to sit for 5 min before gently rinsing the amyloid deposited on glass with 50 µL of distilled water (x3). Samples were then blown dry with a gentle stream of compressed N_2 and cover slipped.

2.2.2 Mueller matrix polarimetry

An inverted transmission Nikon microscope was modified for polarimetric imaging to detect the interaction of retinal deposits with polarized light. A polarization state generator (PSG) and a polarization state analyzer (PSA) were placed before and after the sample, respectively. Both the PSG and PSA are composed of a linear polarizer and a quarter wave plate (QWP), with the polarizer followed by a QWP in the PSG and the opposite in the PSA. The light travels from the PSG through the sample to the PSA before being collected by the camera (Fig 2.1).
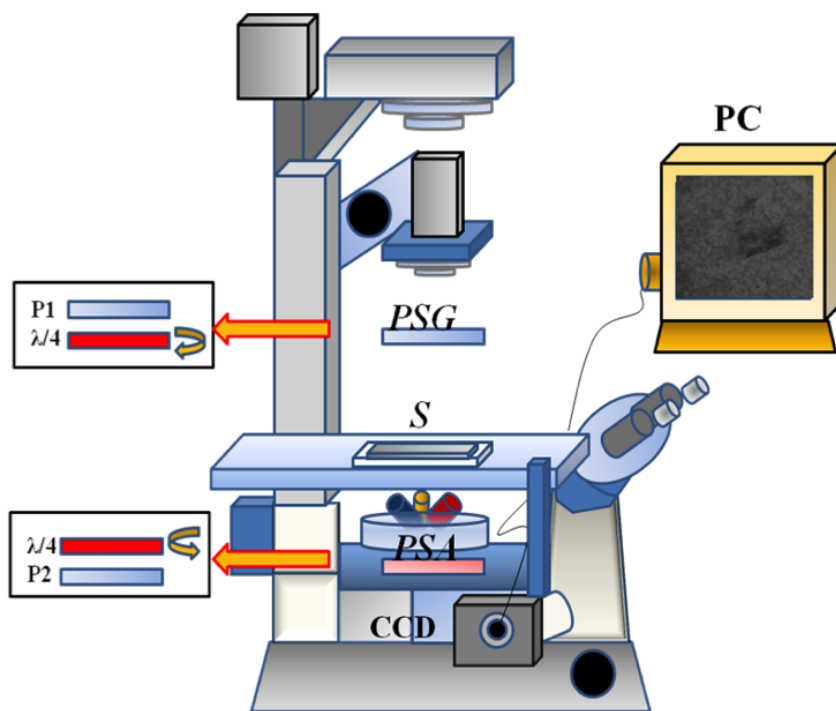
Figure 2.1. A schematic diagram represents the setup of the microscope channel for polarimetric imaging. P1 and P2 are linear polarizers, $\frac{\lambda}{4}$ marks quarter wave plates. The CCD is a camera with a charge-coupled device.

The QWP in the PSG is rotated to 4 angles (45˚, 0°, -30˚, and -60°) to generate 4 different input polarization states. The output at each setting was determined by rotating the QWP in the PSA to the same 4 angles. Thus, a combination of 16 measurements were performed for each sample. The

19

images obtained were registered to compute the Mueller matrix of the sample at each image pixel. The intensity, I_i recorded in the ith measurement is then,

$$I_i = M_{PSA,i} M_s M_{PSG,i} S_{in} \ (i = 0,1,2, \dots, 15) \tag{2.1}$$

where S_{in} stands for the Stokes vector of the incident light; $M_{PSA,i}$ and $M_{PSG,i}$ are the Mueller matrices of the PSG and PSA. Since the Mueller matrices of these elements are known, the Mueller matrix of sample, M_s, can be determined. This analysis was performed by Erik Mason.

2.2.3 Machine learning approach

I undertook the machine learning analysis. Means and standard deviations of polarimetric properties (features) of the segmented deposits were used as feature inputs for machine learning algorithms which then learn to classify the deposits as members of the thioflavin positive or negative datasets labelled by their class. Thus, the algorithms are often referred to as classifiers.

For definitions of machine learning terms please refer to Appendix 1.

2.2.4 Segmentation and calculation of properties of polarimetric images

From the 16 element Mueller matrix calculated at each pixel, the state of polarized light exiting from the sample for each possible state of light input can be calculated. The way in which the input polarized states are changed to the exiting states is described by the Mueller matrix of each pixel of the sample which can then be expressed as polarimetric properties. For example, one state of incident polarization could be preferentially absorbed (the property of diattenuation) or the refractive index seen by different polarizations could differ (the property of retardance) or polarized light could be changed to partially polarized light[40].

For each deposit, the mean and standard deviation (STD) of 14 polarimetric properties were extracted from the Mueller matrix values of the segmented pixels and used as feature inputs for machine learning algorithms. Linear retardance (LR), circular retardance, and depolarization power were extracted by the polar decomposition method[7]. Two polarimetric properties, linear anisotropy (LA) and circular anisotropy, were calculated from the Mueller matrix components[41]. Four polarimetric properties computed by the Mueller matrix transformation technique were:

metric A (a measure of LA), metric b (sensitive to small sources of scattered light in samples), metric t (related to the magnitude of the anisotropy) and metric x (related to the direction of the aligned fibrous structures)[42,43]. Linear and circular polarizance and diattenuation were directly obtained from the polarizance and diattenuation vectors of the Mueller matrix. The Q metric is a polarimetric property which contains information on depolarization, polarizance and diattenuation[44]. Table A1 in Appendix 2 summarizes all 14 polarimetric properties with equations. Polarimetric properties of presumed amyloid deposits (plotted as images) were segmented from the surrounding retinal background by a custom polarimetry segmentation method (Erik Mason, et al. IOVS 2019;60:ARVO E-Abstract 179).

2.2.5 Oversampling methods for solving data imbalance

As described in Section 2.1, our two datasets do not have balanced deposit numbers (789 fluorescence positive and 131 fluorescence negative deposits). In this study, the minority (smaller) dataset contains samples with polarization signals but no fluorescence signals, and the majority (larger) dataset contains samples with both polarization and fluorescence signals. This imbalance, frequently observed in medical datasets, can lead to poor performance of most classification algorithms[45]. Two oversampling methods were used to resolve data imbalance while maintaining the information of the original dataset: 1) sampling fluorescence negative retinal background and 2) the borderline-SMOTE algorithm[46].

2.2.5.1 Method 1: Retinal oversampling–adding the surrounding retinal background

To supply more samples with no fluorescence signal, regions with the same shape as a polarimetric positive deposit in a nearby fluorescence and polarimetric negative retinal region were extracted (Fig. 2.2). The extracted region has no fluorescence signal and a weak polarization signal. We then calculated the mean and STD of the polarimetric signals from these regions and labeled them as non-fluorescence deposits. 658 of the above regions were randomly selected from the eligible retina areas. As a result, we have an equal number (789) of fluorescence positive and fluorescence negative samples after oversampling.
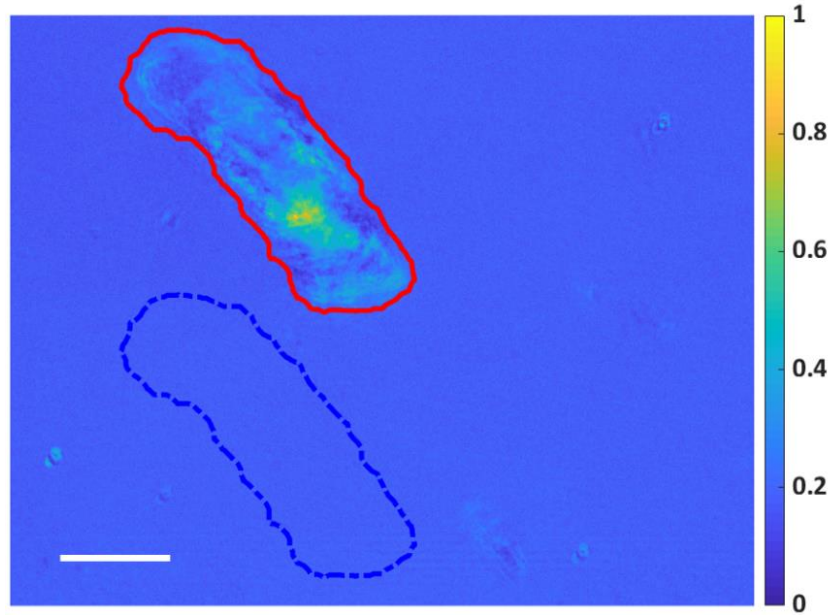
Figure 2.2. An example of the retinal oversampling method. In the linear anisotropy image of a polarimetric positive deposit, a region with the same shape (blue dashed line) as the deposit (red line) with no fluorescence signal is extracted as a fluorescence negative sample. Scale bar: 20 μ.

2.2.5.2 Method 2: oversampling by borderline-SMOTE

Another way of oversampling is to artificially generate data to add to the minority dataset. Here, an improved version of the SMOTE algorithm[47] – borderline-SMOTE[46] was applied. This algorithm first performs k-nearest neighbor analysis on the thioflavin negative (minority) dataset where the nearest neighbors may be within either or both minority and thioflavin positive (majority) datasets. Based on the type of nearest neighbors, deposits in the minority dataset are ranked into three subsets: noise, danger and safe. Deposits in the noise subset have all nearest neighbors in the majority dataset; deposits in the safe subset have more than half of their nearest neighbors in the minority dataset. These subsets are relatively far from the border between the minority and majority datasets. Deposits in the danger subset have more than half but not all of their nearest neighbors in the majority dataset. A certain number of new synthetic data is generated by performing SMOTE algorithm only on the danger subset.

2.2.6 Applying machine learning algorithms

Since different polarimetric properties have different scales due to their nature (e.g. LR ranges from 0° to 180° while linear diattenuation ranges from 0 to 1), a widely used method called min-max scaling which converts all polarimetric properties to have the same scale using formula (2) was applied to standardize polarimetric property scales.

$$X_{scaled} = \frac{X - X_{min}}{X_{max} - X_{min}} \tag{2.2}$$

where X_{min} and X_{max} represent the minimum and maximum theoretical values of a given polarimetric property.

The rescaled combined thioflavin negative and thioflavin positive polarimetric datasets were then randomly split into two sets for training (80%) and testing (20%). During training, 10-fold cross-validation was performed to evaluate the accuracy and robustness of the classifiers[48]. Three different algorithms were trained to automatically determine the existence of a fluorescence signal: linear discriminant analysis (LDA), SVM and RF. The hyper-parameters (input settings, Appendix 2: Table 2) of SVM and RF were optimized by the randomized search function provided in the scikit-learn library[49], which selects random combinations in a grid of hyper-parameters to train the model and return the combination with the best accuracy.

Apart from the mean accuracy (ACC) returned from 10-fold cross-validation, we also evaluated the performance of each trained algorithm (classifier) by computing sensitivity (SEN), specificity (SPE) and area under the receiver operating characteristic curve (AUC) on the test set. The evaluations were repeated 5 times to establish STDs. A receiver operating characteristic (ROC) curve was calculated for each classifier to compare their classification performance[50].

Finally, the variable importance[51] was obtained from the RF analysis to assess the importance of each polarimetric property in predicting deposit fluorescence. The variable importance is calculated by the average decrease of the Gini impurity when each property is considered. At each node τ, the Gini impurity is calculated as,

$$Gini(\tau) = 1 - \sum_k p_k{}^2 \tag{2.3}$$

23

where k stands for the class (or label) of each dataset, fluorescence positive or fluorescence negative; P_k stands for the proportion of the sample placed in class k before and after splitting at a node. The property with the smallest Gini impurity is chosen for node splitting.

2.3 Result

2.3.1 Visualization of retinal deposits

A Mueller Matrix of a polarimetric and fluorescence positive deposit is shown in Appendix Fig A1. The deposit is clearly visible against the surrounding retina.
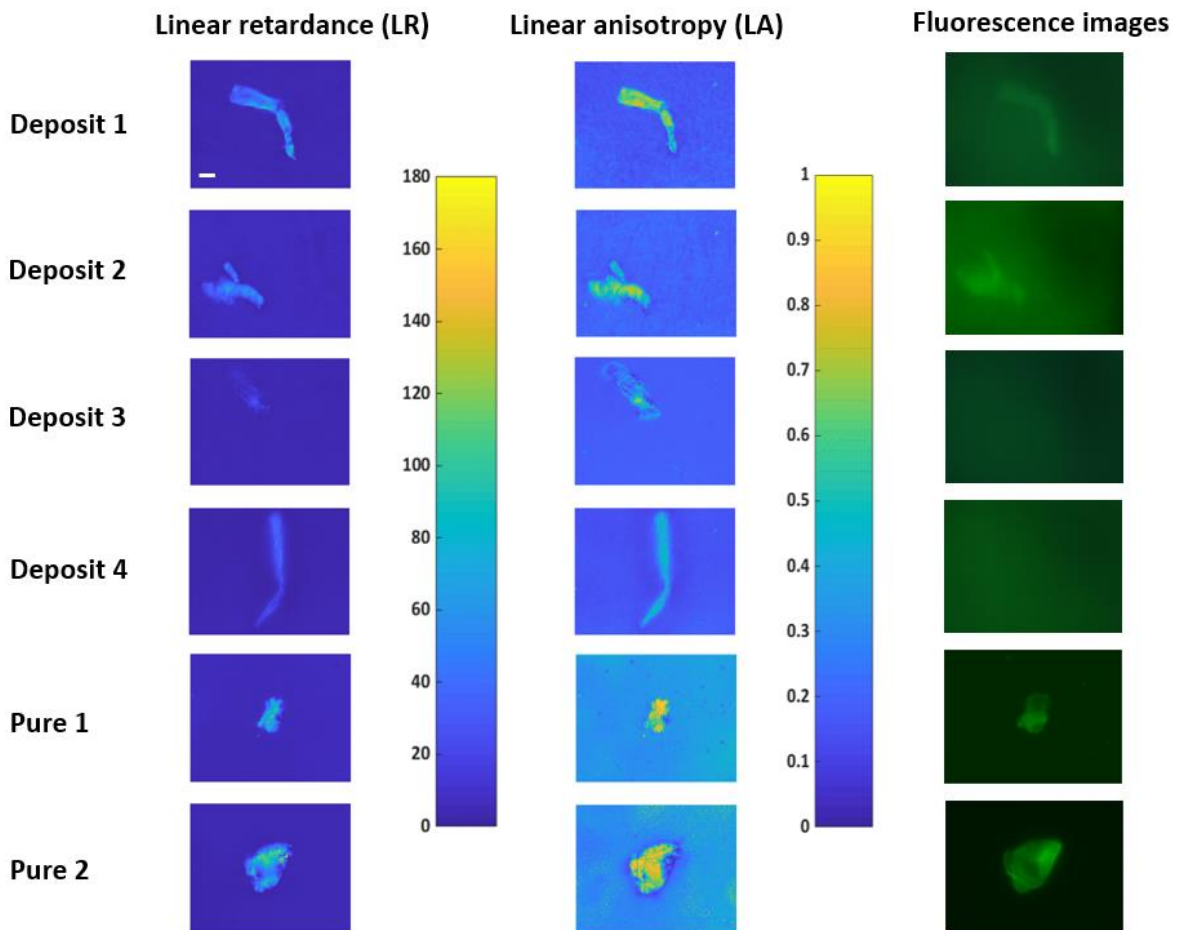
Figure 2.3. Linear retardance (LR), linear anisotropy (LA) and fluorescence images of four retinal deposits (1 and 2 have fluorescence signals while 3 and 4 do not) and two pure Aβ-42 proteins with fluorescence signals. Range of LR: [0°, 180°], LA: [0, 1]. Scale bar in the upper left panel: 20 μ.

Four examples of the polarimetric properties of retinal deposits (two fluorescence positive and two fluorescence negative) are displayed in Fig. 2.3. In general, these polarimetric properties change pixel-to-pixel as well as between deposits and surrounding retina. These deposits have signals in polarimetric properties including LR and LA. Retinal deposits 1 and 2 and both pure protein deposits are positive for thioflavin fluorescence. The distributions of the strength of polarimetric properties across retinal deposits differ between fluorescence positive and negative deposits but are similar between fluorescence positive retinal deposits and pure proteins. Using machine learning algorithms, our aim was to identify the differences in polarimetric properties between fluorescence positive and negative retinal deposits and predict the existence of a fluorescence signal.

Initially, 16 deposits appeared to be fluorescent positive and polarization negative but a comparison of the averages of polarization signals from each deposit and surrounding retina found that 3 deposits had weak polarization signals. None of the 16 deposits were included in the datasets.

2.3.2 Performance of the three algorithms in classification

The performance of the three algorithms (LDA, SVM and RF) in classification was assessed using three different methods (without oversampling, retinal oversampling method and oversampling by borderline-SMOTE) and the outcomes are shown in Table 1. The AUCs are summarized in Table 2 and the ROC curves are shown in Fig. 2.4.

Table 2.1. ACC, SEN and SPE of the three machine learning classifiers under three sampling strategies

Method	Without oversampling			Retinal oversampling			Borderline-SMOTE oversampling		
	ACC	SEN	SPE	ACC	SEN	SPE	ACC	SEN	SPE
LDA	90.3 ± 0.7%	96.6 ± 2.1%	47.5 ± 3.9%	90.9 ± 0.0%	91.1 ± 3.1%	93.4 ± 1.2%	80.5 ± 0.7%	76.8 ± 1.4%	85.4 ± 2.4%
SVM	85.9 ± 0.7%	100.0 ± 0.0%	0.0 ± 0.0%	92.5 ± 0.3%	95.6 ± 0.7%	91.4 ± 0.7%	93.1 ± 0.5%	91.0 ± 1.2%	95.0 ± 1.1%
RF	91.3 ± 0.8%	97.0 ± 2.2%	45.9 ± 1.5%	93.7 ± 0.2%	95.5 ± 1.3%	92.1 ± 2.1%	94.6 ± 0.8%	93.6 ± 2.1%	96.7 ± 0.77%

The means ± standard deviations are given for each of accuracy (ACC), sensitivity (SEN) and specificity (SPE) for each of linear discriminant analysis (LDA), supporting vector machine (SVM) and random forest (RF), without oversampling and with two different oversampling methods.

ACC is the mean accuracy from 10-fold cross-validation. Shown are the mean values with STDs obtained from shuffling and recalculating the training and test sets 5 times. From Table 1, the SPEs of all classifiers are significantly improved after applying oversampling methods. Among the three classifiers, the performance of LDA is the most sensitive to the choice of oversampling method, with ACC, SEN and SPE dropping by 11% on average in the borderline-SMOTE method compared with retinal oversampling. SVM had lower SEN but higher SPE in borderline-SMOTE oversampling, giving a negligible change in ACC. Both SVM and RF perform well and are relatively insensitive to the oversampling method with ACC of RF slightly above SVM at 94-95%.

Table 2.2. Summary of AUC of the ROCs of the three machine learning classifiers under three sampling strategies

Method	Without oversampling	Retinal oversampling	Borderline-SMOTE oversampling
	AUC	AUC	AUC
LDA	0.863 ± 0.015	0.958 ± 0.003	0.885 ± 0.011
SVM	0.859 ± 0.019	0.967 ± 0.008	0.975 ± 0.003
RF	0.880 ± 0.019	0.981 ± 0.006	0.986 ± 0.007

The area under the receiver operating characteristic curve (AUC of the ROC) is shown ± its standard deviation for each of the 3 classifiers: linear discriminant analysis (LDA), support vector machine (SVM) and random forest (RF) without and with two oversampling methods, retinal oversampling and borderline-SMOTE oversampling.
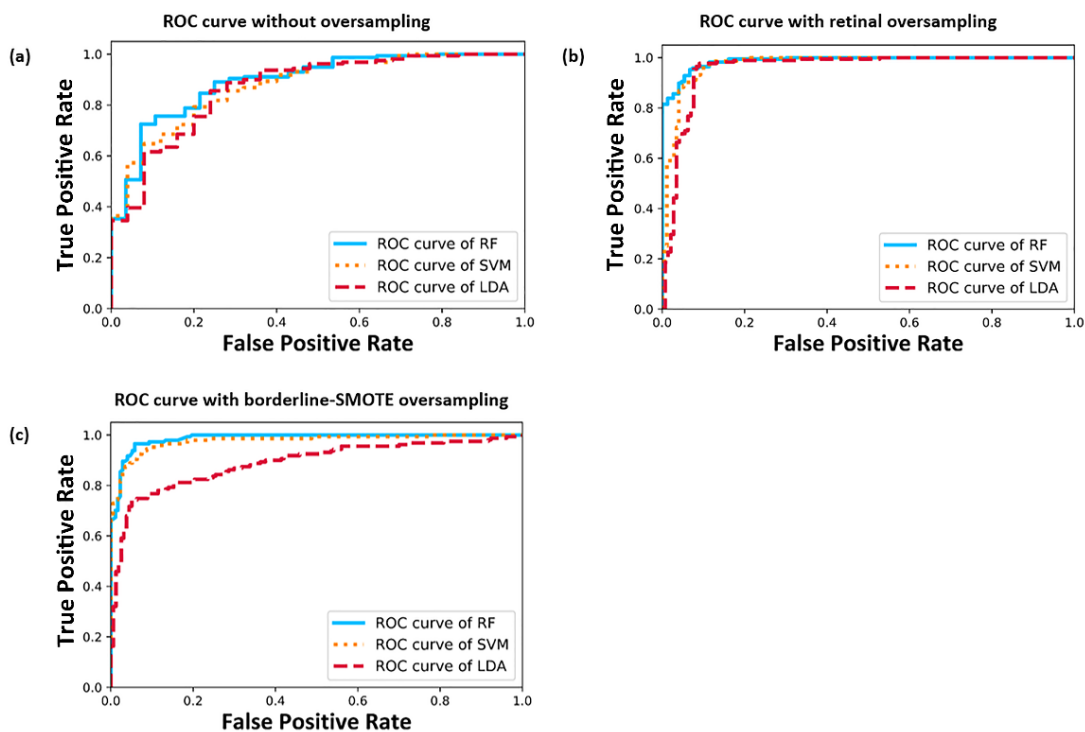
Figure 2.4. Receiver operating characteristic (ROC) curves for fluorescence signal prediction by the three classifiers under three sampling strategies. True positive rate is sensitivity and false positive rate is 1-specificity.

Overall, the AUCs of the three classifiers in Table 2.2 increased after using oversampling methods, from previously lower than 90% to more than 95%, except for the LDA classifier in the borderline-SMOTE method which was not different from before oversampling. The AUC values for the RF and SVM classifiers were not significantly different between the two oversampling methods. The RF classifier has the highest AUC in comparison to LDA and SVM using the borderline-SMOTE oversampling (AUC=0.986).

2.3.3   Importance of polarimetric properties

We ranked the polarimetric properties by their importance as feature inputs in RF analysis in Fig. 2.5 for retinal oversampling and in Fig. 2.6 for the borderline-SMOTE oversampling method.

27
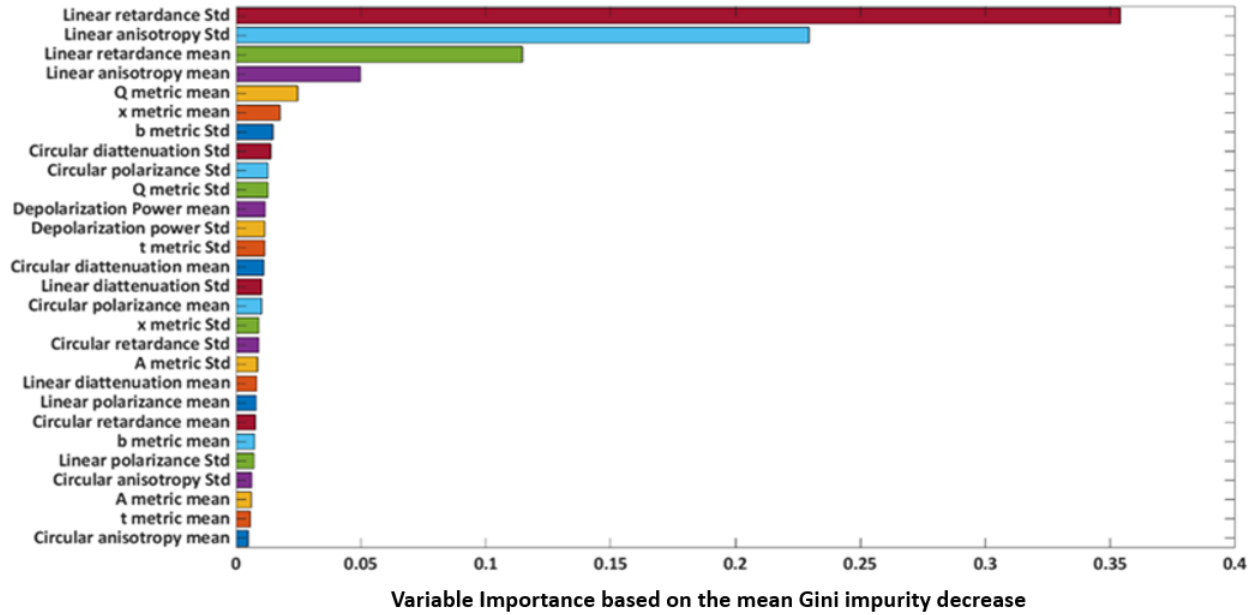
Figure 2.5. The variable importance of 28 polarimetric properties as feature inputs (mean and standard deviation of 14 polarimetric properties) from RF analysis with retinal oversampling. The sum of the variable importance of all features is 1.
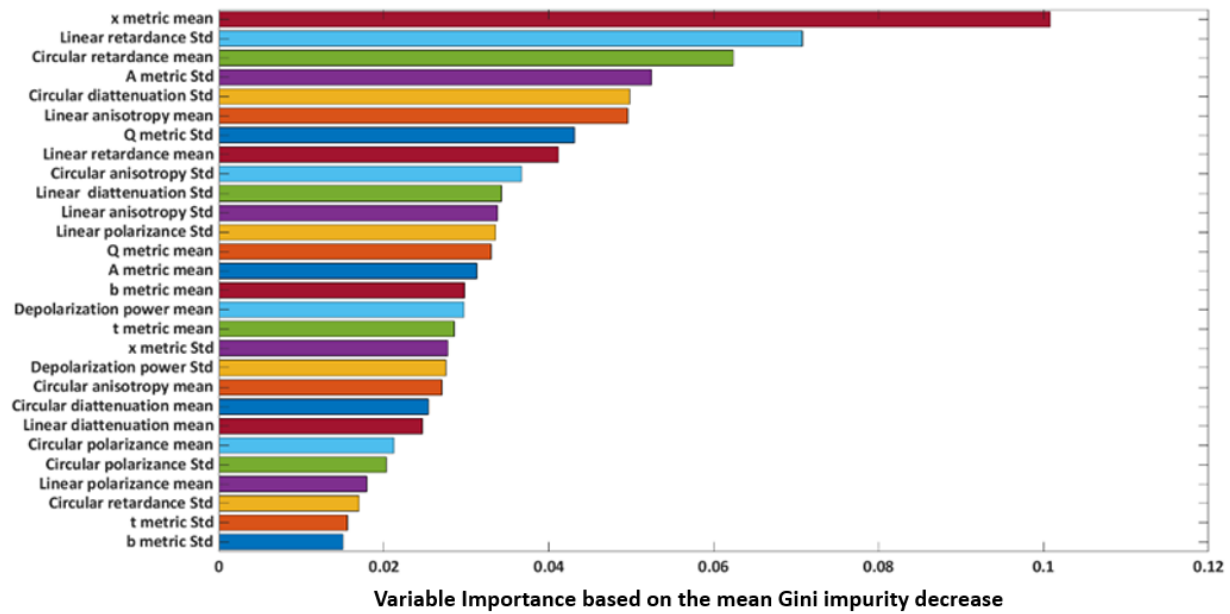
Figure 2.6. The variable importance of 28 feature inputs (mean and standard deviation of 14 polarimetric properties) for RF analysis with borderline-SMOTE oversampling. The sum of the variable importance of all feature is 1.

In retinal oversampling (Fig. 2.5), LR and LA were two dominant polarimetric properties (features) in predicting Thioflavin-S fluorescence. Their means and STDs together accounted for 74.8% of the total variable importance. Therefore, other feature inputs with lower importance were excluded, and the analysis was rerun with only mean and STD of these 2 polarimetric properties as feature inputs. Table 2.3 summarizes the results of retinal oversampling before and after this selection.

Table 2.3. Classification performance by retinal oversampling before and after applying feature selection

Method	Retinal oversampling method					
	Before feature selection			After feature selection		
	ACC	SEN	SPE	ACC	SEN	SPE
LDA	$90.9 \pm 0.0\%$	$91.1 \pm 3.1\%$	$93.4 \pm 1.2\%$	$89.1 \pm 0.3\%$	$84.5 \pm 3.4\%$	$94.4 \pm 1.6\%$
SVM	$92.5 \pm 0.3\%$	$95.6 \pm 0.7\%$	$91.4 \pm 0.7\%$	$92.4 \pm 0.3\%$	$94.0 \pm 1.4\%$	$92.0 \pm 2.1\%$
RF	$93.7 \pm 0.2\%$	$95.5 \pm 1.3\%$	$92.1 \pm 2.1\%$	$92.8 \pm 0.5\%$	$94.9 \pm 0.7\%$	$91.4 \pm 2.4\%$

The average accuracy (ACC), sensitivity (SEN) and specificity (SPE) ± standard deviation before feature selection (with all polarimetric properties included) and after feature selection (with a small subset included) for each of the 3 classifiers: linear discriminant analysis (LDA), support vector machine (SVM) and random forest (RF) for the retinal oversampling method.

From Table 2.3, there was a decrease in the ACC and SEN for LDA; and a small decrease in ACC for RF but no other significant changes after performing feature selection. Although only four polarimetric properties were used as features, SVM and RF classifiers still achieved over 90% in ACC. Thus, other polarization metrics can be excluded to speed up the analysis with little loss in performance in predicting deposit florescence.

In contrast, the variable importance distribution of each polarization feature was much different under borderline-SMOTE oversampling in Fig. 2.6 than in retinal oversampling with a much smaller range of contribution values (contributions range from 1.5% to 10.1%). Therefore, feature selection was not applied for the borderline-SMOTE oversampling method as there was no evidence of dominant polarimetric properties.

29

2.4 Discussion

There are some limitations in this study. Firstly, it is difficult to quantitatively evaluate the similarity between an oversampled dataset and the actual dataset. This may affect the generalization and robustness of our models. Because retinal deposits are found sparsely distributed across the retina, retinal oversampling is justified. Although more data from retinal deposits with polarimetric but no fluorescence signals would further validate the reliability of the oversampling methods, since polarimetry predicts thioflavin positivity with high accuracy, such false negative deposits are scarce.

Secondly, the limited number of retinas (28) and deposits (920, before oversampling) involved in this study could bias our models. Thus, it would be helpful to analyze more retinas to enhance the generalization of the models before moving to a clinical setting. However, the number of paired retinas and brains available post-mortem are limited. *In vivo* studies could compare retinal polarimetry and *in vivo* brain amyloid measurements in larger sample sizes.

Thirdly, other classification models such as convolutional neural networks should be tested to see if they can further improve the already excellent accuracy of the classification of thioflavin positive (presumed amyloid) versus thioflavin negative deposits. Considering the accuracy as well as the computation/memory and time costs of the models, we could then select the one that would be best for clinical application.

Amyloid stained with Congo red is known to interact with polarized light producing an apple green birefringence signal[52,5]. We have shown that unstained pure amyloid-β and thioflavin positive retinal amyloid deposits also interact with polarized light and show very similar variations of LR and depolarization across deposits (Corapi F, *et al*. IOVS 2018;59:ARVO E-Abstract 1582). These similarities and thioflavin positivity[53] are presumably due to the fibrillary, well-ordered structure of these deposits[53]. Thus, it is not unexpected that LR and polarimetric properties which are related to LR (such as LA) are important to distinguishing thioflavin positive (amyloid) deposits from those that are not thioflavin positive.

Amyloid deposits show a range of polarimetric property strength, both within and between deposits, potentially due to a variety of factors including: variations in thickness (thinner regions have weaker signals, usually at the edge of deposits (e.g. deposit 2 in Fig. 3), in the uniformity of

orientation of the fibrils and potential differences in amyloid species. Thioflavin has been known to stain amyloid species other than amyloid-β, such as alpha-synuclein[32]. By choosing retinas from donors with a brain pathology of amyloid deposits of the Alzheimer's type, we expect the majority of thioflavin positive deposits to contain amyloid-β. The lack of polarization signals for a small number (16) of thioflavin positive deposits may indicate one or more of the following: thinner deposits (Tao Jin, *et al.* IOVS 2017;58:ARVO E-Abstract 3367), more disordered deposits or the presence of other impurities (analogous to neuritic material found in brain plaques)[54].

Despite the range of polarimetric properties of deposits in the retina which indicates differing interactions with polarized light, in the present study, we trained machine learning classifiers to precisely and robustly distinguish polarimetry positive retinal deposits with and without thioflavin fluorescence signals. In turn, thioflavin positivity defines a presumed amyloid deposit. In this study, the RF and SVM classifiers exhibited high accuracy, sensitivity and specificity. Two oversampling methods proved to be useful for dealing with the larger numbers of fluorescence positive versus negative deposits and improved the specificity, AUC and, in all but one case, the ACC of the classifications.

Using the RF algorithm with the retinal oversampling method, we found that the means and STD of two polarimetric properties, LR and LA, have superior performance in predicting fluorescence positivity. We can use only these four properties as feature inputs to produce excellent classification performance. From the perspective of the physical meanings of these two polarimetric properties, LR is directly related to the linear birefringence which results from the ordered alignment of the fibrils. LA is a measure of the polarimetric anisotropy of samples, which can be interpreted as the different optical responses to light polarized in different directions caused by the samples' LR and linear diattenuation[41,55]. LA is postulated to have a periodic variation that reflects the geometric structure of samples[41] such as the orientation of fibrillary structures. The high importance of these two polarimetric properties suggests that the ordered arrangement of fibrils may be the key to distinguishing between fluorescence and non-fluorescence deposits. Given the similarities between LR and LA patterns in deposits in Fig. 2.3, for amyloid, retardation appears to contribute more to LA than diattenuation.

In the case of the second (borderline-SMOTE) oversampling method, the variable importance returned from RF analysis indicates that LA and LR are no longer dominant variables. The

contributions of all variables are within one order of magnitude. This difference in variable contribution is likely caused by the differing data introduced by the two oversampling methods. We performed a t-distributed stochastic neighbor embedding (t-SNE) [56] (see Appendix) to show the distributions of the polarimetric properties of each deposit for each oversampling method. The t-SNE algorithm maps the local distance information from the original high-dimensional space (of 14 properties) to a two low-dimensional space. Perplexity, whose value is varied, provides a smooth measurement of the number considered as neighbors, which alters the algorithm's attention on local and global information (local variations dominate at a small perplexity). The t-SNE visualization plots for differing values of perplexity are displayed in Fig. 2.7a for the retina oversampling method and Fig. 2.7b for the borderline-SMOTE oversampling method.
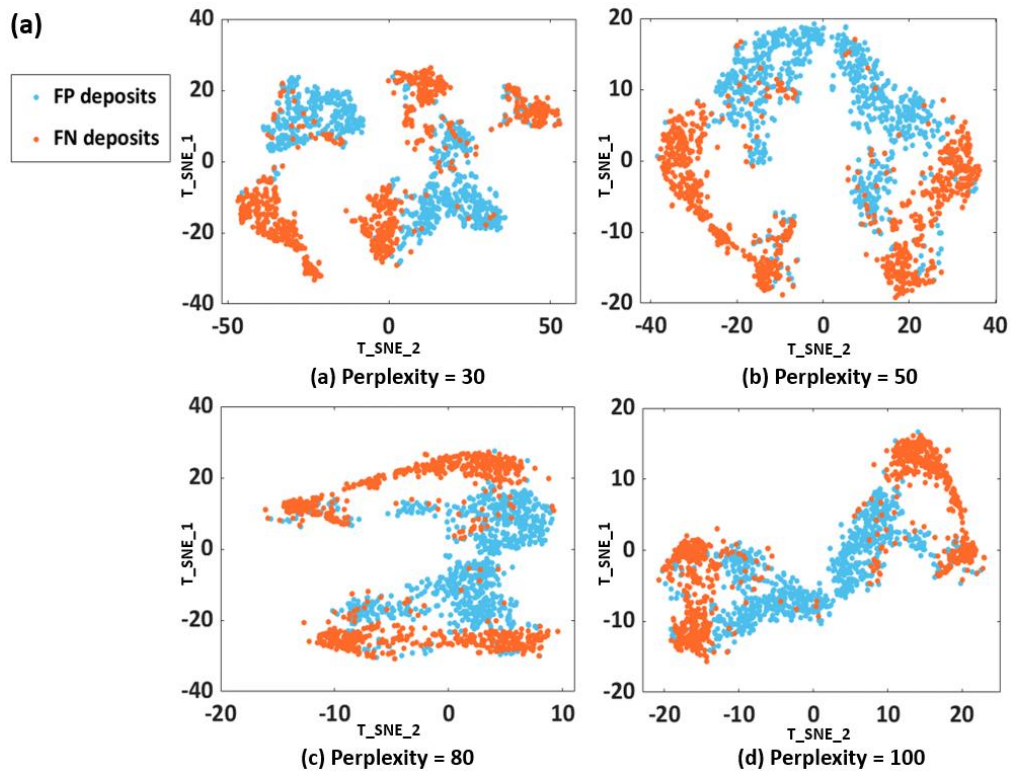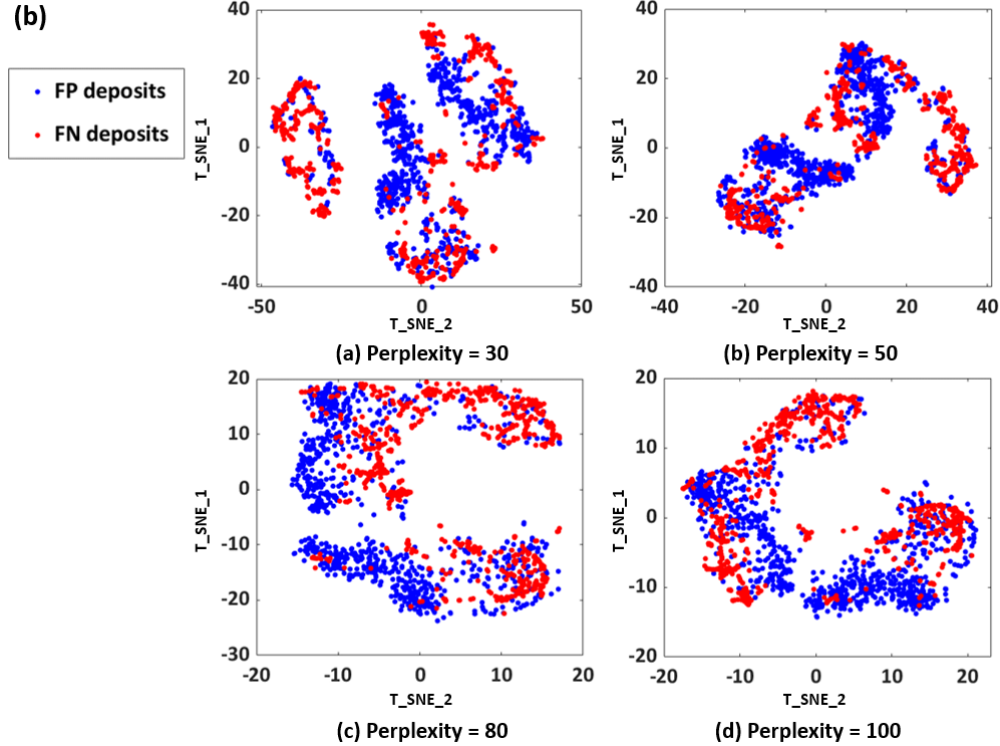
Figure 2.7. Two-dimensional t-SNE visualization of the polarization properties of the fluorescent positive and fluorescent negative datasets from a) the retinal oversampling method and b) the borderline-SMOTE oversampling method under different values of perplexity. The distribution focus moves from the local to the global as the perplexity increases. FP and FN are fluorescent positive and negative deposits respectively. T_SNE_1 and T_SNE_2 are the axis of the two-dimensional space to which the t-SNE mapped the higher dimensions.

We can see in the t-SNE perplexity plots (Figs 2.7a and 2.7b), that the data points of fluorescent negative and fluorescent positive areas are somewhat more separated in the retinal oversampling method than in the borderline-SMOTE oversampling method. As the perplexity increases, the sample distribution with negative fluorescence in retinal oversampling tends to aggregate at both ends of the dataset, while the borderline-SMOTE oversampling method produces a more complex data distribution. This implies that the properties of deposits identified in the borderline-SMOTE oversampling are closer to those of the fluorescent positive deposits than in retinal oversampling. The differing data distributions are consistent with lower accuracy for LDA with borderline-SMOTE. It is also not surprising that for the two oversampling methods, differing polarimetric properties differentiate fluorescent positive from fluorescent negative deposits.

The methods described here predict from the polarimetric properties of retinal deposits, with high accuracy, the existence of amyloid with thioflavin positive fluorescence signals. We have shown

that, in combination with machine learning algorithms, imaging using Mueller matrix polarimetry can detect amyloid positive deposits in the *ex vivo* retina without using a dye. We have previously reported that the polarimetric signals from retinal amyloid deposits measured in double pass, analogous to the live eye imaging method proposed in Campbell's patents[57], give polarimetric signals which are twice as large as those seen in single pass measurements (Photonics North presentation, 2016). Our preferred live eye implementation uses a confocal scanning laser ophthalmoscope combined with polarimetry. Using the methods described here, we expect that thioflavin positive retinal deposits could be identified with high accuracy in live-eye imaging. In turn, we have previously shown that the number of retinal amyloid deposits predicts the severity of amyloid in the brain[31]. Therefore, *in vivo* dye-free polarimetric imaging of deposits in the retina could determine brain amyloid non-invasively, in contrast to current invasive methods. The results reported here are an important step towards development of a novel, non-invasive, clinical method of imaging retinal amyloid as a predictor of brain amyloid.

Chapter 3

3 Differentiating pure Amyloid Beta-42 and Alpha-Synuclein proteins by a convolutional neural network

3.1 Introduction

In the previous two chapters, I have introduced the use by our group of Mueller matrix polarimetry to detect amyloid deposits on the retina as a promising method to achieve the early diagnosis of AD. Since thioflavin fluorescence is the gold standard for the detection of amyloids, we developed machine learning algorithms to predict the fluorescence signal of a retinal deposit from the polarimetric signals. This determines if that detected deposit is a presumed amyloid deposit, and, because it uses polarimetric properties, it avoids the use of a dye in *in vivo* live-eye imaging. However, another protein called alpha-synuclein (alpha-syn) contains a β-sheet structure and amyloid-like fibrils[58], thus also may be positive in thioflavin staining[58]. Similar to amyloid beta (Aβ), a biomarker of Alzheimer's disease (AD), alpha-syn can also aggregate to form an intraneuronal proteinaceous inclusion called Lewy bodies which are associated with a number of neurodegenerative disorders other than AD[59]. It is generally believed that the formation of Lewy bodies is associated with Parkinson's disease (PD)[59]. Studies have also shown that Lewy body brain pathology may exist in AD patients[60–62], and a synergistic interaction may exist between Aβ deposits found in AD and alpha-syn which affects the progression of AD[59]. In either case, it is important to determine whether the protein deposit detected from polarimetric images is Aβ or alpha-syn. Currently, the method to distinguish between alpha-syn and Aβ mainly depends on immunohistochemistry, which involves the process of binding antibodies to specific proteins[63]. This method is often toxic and not very efficient in *in vivo* live eye imaging. A method that can make a real-time judgment through imaging will have a promising application in live eye imaging.

Since 2010, the ImageNet Large Scale Visual Recognition Challenge (ILSVRC) has been held. With the help of the huge dataset provided by this project, which includes more than 1 million images from more than 20000 categories[64], the convolutional neural network (CNN)'s ability to recognize images has been significantly boosted and it soon outperformed other algorithms[65]. The success of CNN on ImageNet has been applied to the field of medical diagnosis. For example one study used a CNN architecture with four convolutional layers and two fully connected layers to diagnose glaucoma in the retina on two glaucoma datasets (ORIGA and SCES)[66]. Another used a thirteen-layer CNN architecture on brain electroencephalogram signals to diagnose PD[67]. They both achieved a decent accuracy but also have a common feature: the architectures of CNNs are not deep enough. In 2015, Kaiming He *et al.* found that increasing the depth of CNNs by simply stacking multiple layers did not improve the performance of the networks[68]. The deeper network they trained (56 layers) had both higher training and testing errors compared to the 20-layer network[68]. This degradation in the performance of a network when adding more layers is not simply due to overfitting. To solve this problem, Kaiming He *et al.* proposed a new CNN architecture called residual network (Resnet), which won 1st place on the 2015 ILSVRC competition[68]. In optical coherence tomography images of the retina, Resnet was trained to classify abnormalities including cystoid macular edema, serous macular detachment, epiretinal membrane and macular hole[69]. Resnet has also been used to assist in the detection of coronavirus (COVID-19), using chest X-ray radiographs of infected and suspected patients[70].

The purpose of this study was to differentiate protein deposits found in different neurodegenerative conditions. (Aβ-42 is the predominant protein in deposits in AD (with Aβ-40 present to a lessor degree) and alpha-syn deposits predominate in Parkinson's and some other diseases. We wished to differentiate pure deposits of the two proteins, based on their polarimetric images without using immunohistochemistry or other dyes. The ultimate goal is to differentiate retinal Aβ and alpha-syn deposits using a live eye imaging system. Here I start by differentiating deposits of pure Aβ-42 and alpha-syn proteins which others in our group have grown. To this end, I implemented and compared Resnet-based CNN models trained on the images of different polarimetric properties of pure Aβ-42 and alpha-syn.

3.2 Methods

3.2.1 Sample preparation

The preparation of pure Aβ-42 deposits is introduced in section 2.2.1.2. Here, I present the preparation of pure alpha-syn protein deposits by other group members.

250 µL of filtered PBS (pH=7.4) was added to 1 mg of alpha-syn and incubate for two months unagitated at 37°C. Stained alpha-syn was prepared by adding 100 µL of filtered 1.25 mM Thioflavin-T in 80 mM in 100 µL of alpha-syn solution and allowing it to sit for 5 min. Clean glass slides were then drawn through the solution, resulting in deposits of alpha syn on the glass. After being incubated for 15 min under high-humidity conditions created by keeping boiled water in the incubator with the slides, samples were rinsed twice with 50 µL water to remove salt and loosely bound peptide. Samples were then blown dry with a gentle stream of compressed N2 and cover slipped. This procedure was completed by other personnel in the lab.

In this project, 360 pure protein deposits were prepared and analyzed, including 184 containing Aβ-42 and 176 containing alpha-syn. They were then imaged using the Muller matrix polarimetry device introduced in section 2.2.2 to get raw images from which the images representing their various polarimetric properties were calculated. The two polarimetric properties which showed high contrast for thioflavin positive deposits in AD (presumed to contain Aβ) in Chapter 2, LR and LA, were selected to train the CNN. Another property, linear diattenuation (LD) was tested since it exhibited high variable importance in RF analysis for separating Aβ-42 and alpha-syn.

The RF analysis here is similar to the previous analysis in Section 2.2.6, in which means and STDs of 14 polarimetric properties (see appendix 2) of Aβ-42 and alpha-syn were used. The variable importance is evaluated based on the average decrease of Gini impurity[51] when each property was considered.

3.2.2 The Classification model - Resnet 101

The model used in this project to perform CNN, Resnet 101[68], is a type of residual network. The residual network adapts a structure called skip connections to avoid degradation in accuracy as the

depth of the network increases[68]. The schematic of the skip connections in Resnet is shown in Fig 3.1, with a comparison to a regular neural network.

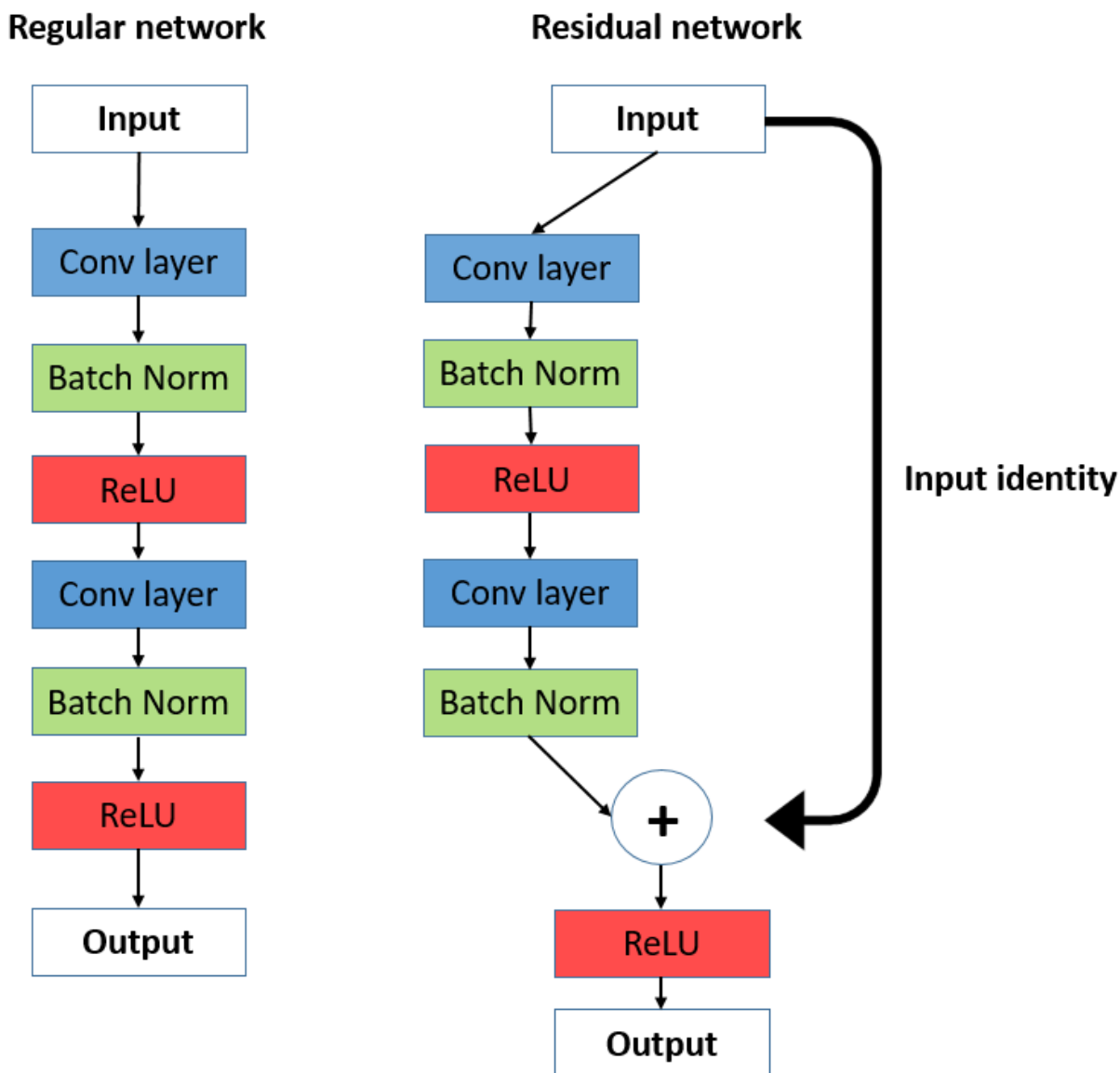**Figure 3.1. Schematics of a regular neural network (left) and a residual neural network with skip connections (right). In the residual network, the identity of input is also added to the output of the stacked layers to get the final output.**

In Fig 3.1, the main difference between the residual network and regular network is that the residual network adds the identity mapping of input x and the output of the stacked layers F(x),

which will force the network to model the target function $H(x) = F(x) + x$ instead of F(x). According to the hypothesize of Kaiming He *et al.*, it is easier to optimize the residual target function $H(x) = F(x) + x$ than to optimize the original target function $F(x)$[68]. One can consider the extreme case where the optimal target function is the identity of the input X, it would be easier to push F(x) close to 0 than to fit F(x) to x by optimizing multiple layers of weights.

With the skip connection, the pre-trained Resnet 101 on ImageNet[64] can go as deep as 101 layers and exhibited excellent performance in ILSVRC competition[68]. Thus it was chosen for use in this project. Its architecture can be summarized as follows[68]:

Table 3.1 The Architectures of Resnet 101, with the skip connections between convolutional layers in convolutional units 2 to 5 [68].

Model name	Resnet 101
Convolutional unit 1	7×7 filter size, depth 64, stride 2, convolutional layer
	3×3 max pooling, stride 2
Convolutional unit 2	$\begin{bmatrix} 1 \times 1, 64, stride = 1 \\ 3 \times 3, 64, stride = 1 \\ 1 \times 1, 256, stride = 1 \end{bmatrix} \times 3$, convolutional layer
Convolutional unit 3	$\begin{bmatrix} 1 \times 1, 128, stride = 1 \\ 3 \times 3, 128, stride = 2 \\ 1 \times 1, 512, stride = 1 \end{bmatrix} \times 4$, convolutional layer
Convolutional unit 4	$\begin{bmatrix} 1 \times 1, 256, stride = 1 \\ 3 \times 3, 256, stride = 2 \\ 1 \times 1, 1024, stride = 1 \end{bmatrix} \times 23$, convolutional layer
Convolutional unit 5	$\begin{bmatrix} 1 \times 1, 512, stride = 1 \\ 3 \times 3, 512, stride = 2 \\ 1 \times 1, 2048, stride = 1 \end{bmatrix} \times 3$, convolutional layer
Average pooling	
One fully connected layer	

Taking the classifier unit in the VGGNet[71] as a reference, four fully connected layers (input size 2048, output size 512), (input size 512, output size 128), (input size 128, output size 32), (input

size 32, output size 2) were added to replace the original fully connected layer (input size 2048, output size 1000), to match the output size with the number of classes (2), with the ReLU layers followed by each. A regulation technique called dropout[72](see appendix) was applied on the last three fully connected layers with dropout rates 0.5, 0.2, 0.2[72], respectively, to prevent overfitting.

3.2.3 Training and evaluating the CNN models

The polarimetric images used in evaluating the CNN models were either [1018 pixels (height), 1269 pixels (width), with 1 channel] or [1018 pixels (height), 1269 pixels (width), with 3 channels. They were then were resized to [224 pixels (height), 224 pixels (width), and 3 channels to fit the input size of Resnet 101. The single channel images were duplicated in the RGB channels to create three channel images. The input image pixels were first min-max scaled to the range of [0, 1], then converted into a standard score[73] by,

$$x_i' = \frac{x_i - \mu}{\sigma}$$

where x_i is the pixel value of an input image i, μ is the average of all input images across all positions, σ is the average of the STD of all input images. Since an average of zero speeds up the convergence to the local optimum[74], μ is set to be 0.5 which is close to the midpoint of the input images range from 0 to 1. σ is also set to 0.5, which will transform the range (0 to 1) to the range (-1 to 1), since a STD of 1 is recommended for efficient convergence[74]. Thus, the average and STD of the scaled input images can be close to 0 and 1, respectively.

The whole image set was split into three subsets for training (252), validation (36) and testing (72) in a ratio of 7: 1: 2. The learning curves for training and validation were plotted with the improvement in accuracies to monitor the performance of network learning and generalizing for each of the 4 different images of polarimetric properties tested. The loss function was computed using the cross entropy loss introduced in section 1.3. The CNNs were trained following the backpropagation rule[12] and SGD[13] (both introduced in section 1.3), with a learning rate = 0.01 and momentum[75] = 0.9. The networks were trained using mini-batch[75] with batch size = 10 and for 100 epochs. The learning rate was set to decay every 5 epochs by multiplying a decay rate of

0.8. This prevented the learning rate from being overly large as training progressed, which would not be conducive to convergence.

In order to compare the performance of maps of different polarimetric properties in classifying Aβ-42 and α-syn, the polarimetric maps (images) of LR, LA and LD were used to train the Resnet 101 models, as well as their combination image which is made by setting the three channels of RGB to be the single-channel images of LR, LD and LA, respectively. The purpose of testing the combination image is to explore whether stacking multiple polarimetric images will improve the performance of CNN, or will average or reduce the performance. In addition, LDA, SVM and RF classifiers were trained and tested following the same procedures described in chapter 2, in order to compare the performance of CNNs with these machine learning techniques.

3.2.4 Visualization the deep inside CNN using saliency map

After training the CNN, it is important to ensure that our model is making decisions based on the features relevant to the proteins. A model with high accuracy but unknown judgments is not what we prefer. Here, a technique called saliency map[76] is used to visualize the "black box" of the neural network by computing the "saliency" (importance) of each pixel in the image to the result.

For a given image I_0, the network will return a score S_c for each class. In our case, the two classes are: Aβ-42 and alpha-syn. The saliency map is made by computing the gradient of the score of the class predicted by the network with respect to each pixel I in I_0.

$$\omega = \left. \frac{\partial S_c}{\partial I} \right|_{I_0}$$

One can note that ω is a gradient map of an image I_0. Intuitively, the gradient describes the ability of each pixel to affect the score. A large gradient for a pixel implies that a small change in that pixel can greatly change the value of S_c. Thus, regions which most contribute to the prediction of the CNN should be highlighted in the saliency map. And if our model works properly, the highlighted region should be related to some features of the protein deposits.

3.3 Results

3.3.1 Visualization and comparison of Aβ-42 and alpha-syn pure protein deposits
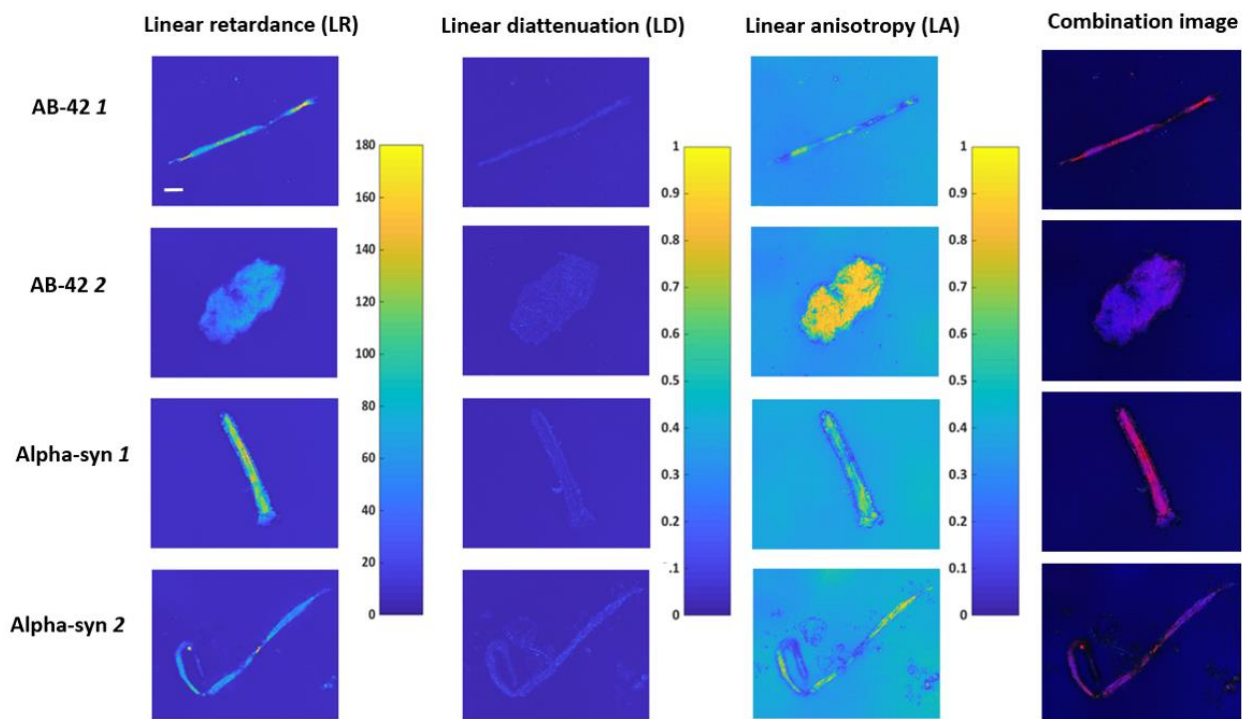
Figure 3.2. LR, LD, LA and a combination images of polarimetric properties (R channel: LR, G channel: LD, B channel: LA) of four pure protein deposits (the top two are Aβ-42 and the bottom two are alpha-syn). Range of LR: [0°, 180°], LA: [0, 1], LD: [0, 1], combination: normalized to [0, 1]. Scale bar in the upper left panel: 20 μ.

Four examples of pure protein deposits are displayed in Fig 3.2; the first two are pure Aβ-42 and the last two are pure alpha-syn. From the morphological point of view, the shapes of the deposits vary not only within protein type but also between proteins. Thus, it is difficult to find a particular rule to distinguish Aβ-42 and alpha-syn morphologically. Aβ-42 and alpha-syn also do not show an obvious difference in their polarization images. Further statistical t-tests confirmed that there were no significant differences between Aβ-42 and alpha-syn in the mean values and STDs of their polarimetric properties including LR ($P = 0.20$ for mean, $P = 0.43$ for STD), LD ($P = 0.06$ for mean) and LA ($P = 0.18$ for mean, $P = 0.76$ for STD), except for the STD of LD ($P = 0.02$) showing a significant difference. The shape-related metrics from blob analysis such as the area, the eccentricity, the major and minor axis, the orientation and the fractal dimension of the deposits were also compared between the Aβ-42 and alpha-syn. Only the fractal dimension shows a

significant difference (P = 0.03) while the P-value of the other metrics are all higher than 0.05. These results suggest that it is difficult to visually or statistically differentiate Aβ-42 and alpha-syn, despite the potential shape difference between the two deposit types given by the fractal dimension. By training CNN, we expect that the network can recognize any shape differences and subtle differences in the distributions of polarimetric properties across deposits of the two types.

The thickness of Aβ-42 and alpha-syn deposits were also compared using a subset on which confocal microscopy was performed to investigate their thickness (40 Aβ-42 and 40 alpha-syn deposits). Welch's t test was used to test the differences in thickness and found no statistically significant difference between Aβ-42 and alpha-syn in thicknesses (P = 0.97). There is also no statistically significant difference in LR for the subset tested for thickness and the larger dataset used for network training.

3.3.2 Classification performance of CNN

The performance accuracy of CNNs trained using the images of different polarimetric properties (LR, LD, LA and a combination of the three) are shown in Table 3.1, and compared with the three machine learning algorithms used in Chapter 2 (LDA, SVM and RF). The training and validation learning curves of the four CNNs are shown in Fig 3.3 and Fig 3.4.

Table 3.2. Table of classification performance of the 7 methods ranked by accuracy

Rank	Method	Accuracy
1	CNN with LR images	90.2 ± 0.3%
2	CNN with LA images	86.2 ± 0.1%
3	CNN with combination images	84.7 ± 1.4%
4	CNN with LD images	76.9 ± 0.8%
5	RF	66.3 ± 1.4%
6	LDA	57.7 ± 0.6%
7	SVM	50.9 ± 0.4%

The accuracies shown are the mean values with STDs obtained from shuffling and recalculating the training and testing sets 3 times. From Table 3.1, the CNN trained by LR images has the highest accuracy around 90%. The accuracy of the CNN trained by LA images is lower than the CNN with

LR images, but higher than the CNN with combination images. The CNN trained by LD images had the lowest accuracy among all the CNNs. The combination image of LR, LD and LA in the RGB channels gives approximately the average performance of each trained separately. All CNNs have better performance than the machine learning methods (RF, SVM and LDA), with the worst-performing CNNs 10% more accurate than the best-performing machine learning method (RF).
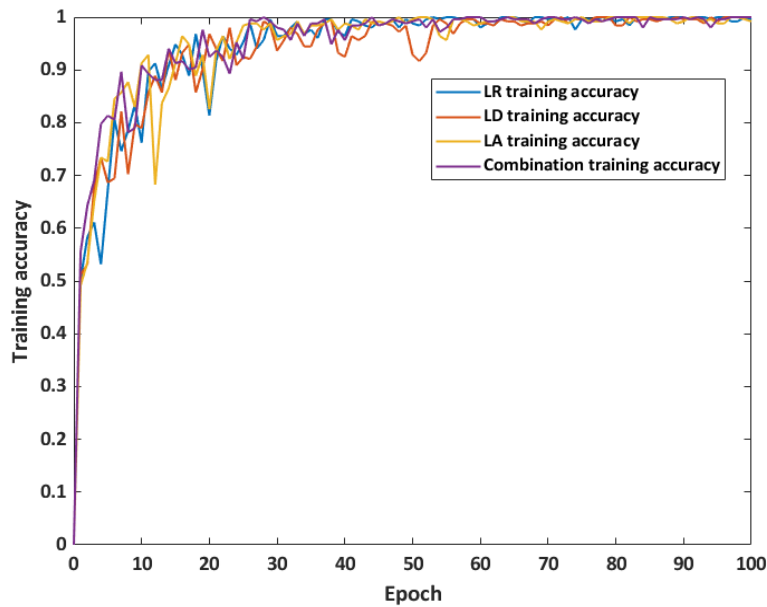

Figure 3.3. The learning curves of the CNNs trained by LR, LD, LA and their combination images over 100 epochs.
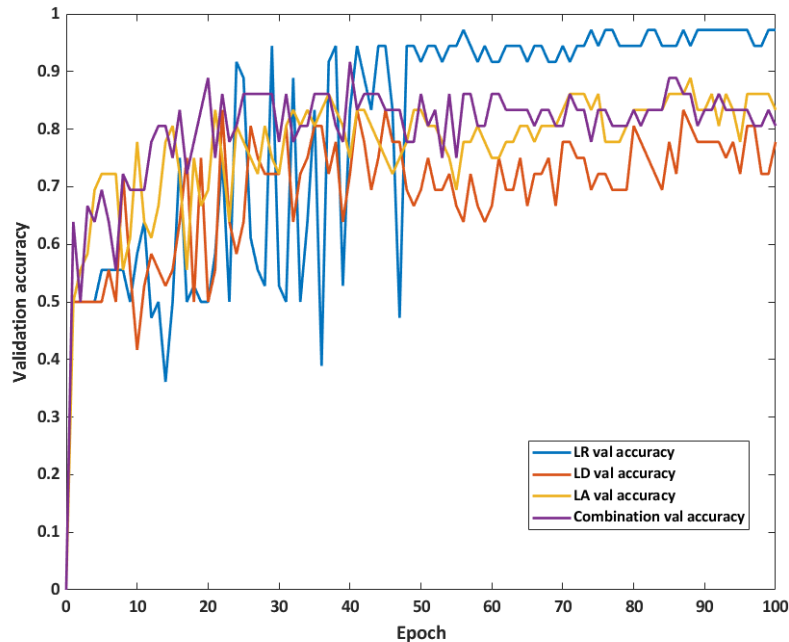
Figure 3.4. The validation learning curves of the CNNs trained by LR, LD, LA and their combination images over 100 epochs.

From Fig 3.3, the training accuracies of four CNNs all improved rapidly in the first 20 epochs and then slowly improved in the next 30 epochs. At the 50 epoch, the training accuracies of the networks were already close to 100%, except the CNN trained by LD which still had relatively large fluctuations. After 100 epoch, all CNNs were stable at 100% training accuracy.

However, the validation learning curves in Fig 3.4 fluctuated more than the training learning curves. The differences between the four CNNs were also more obvious. The LR curve had the most fluctuations in the first 50 epochs, then gradually slowed down and stabilized at above 0.9. The LA and combination curves showed a similar trend, with relatively large fluctuations in the early epochs then reduce to smaller fluctuation around 0.8 in the final epoch. The CNN trained by LD had the lowest validation accuracy, fluctuating between 0.7 and 0.8 after the 85th epoch.

3.3.3 Visualizing and Understanding the network

The saliency maps of four sample protein deposits (two Aβ-42 and two alpha-syn) are shown in Fig 3.5, which are from the CNNs trained with LR, LD, LA and combination images, respectively. The LR images of the protein deposits are also included as a reference.
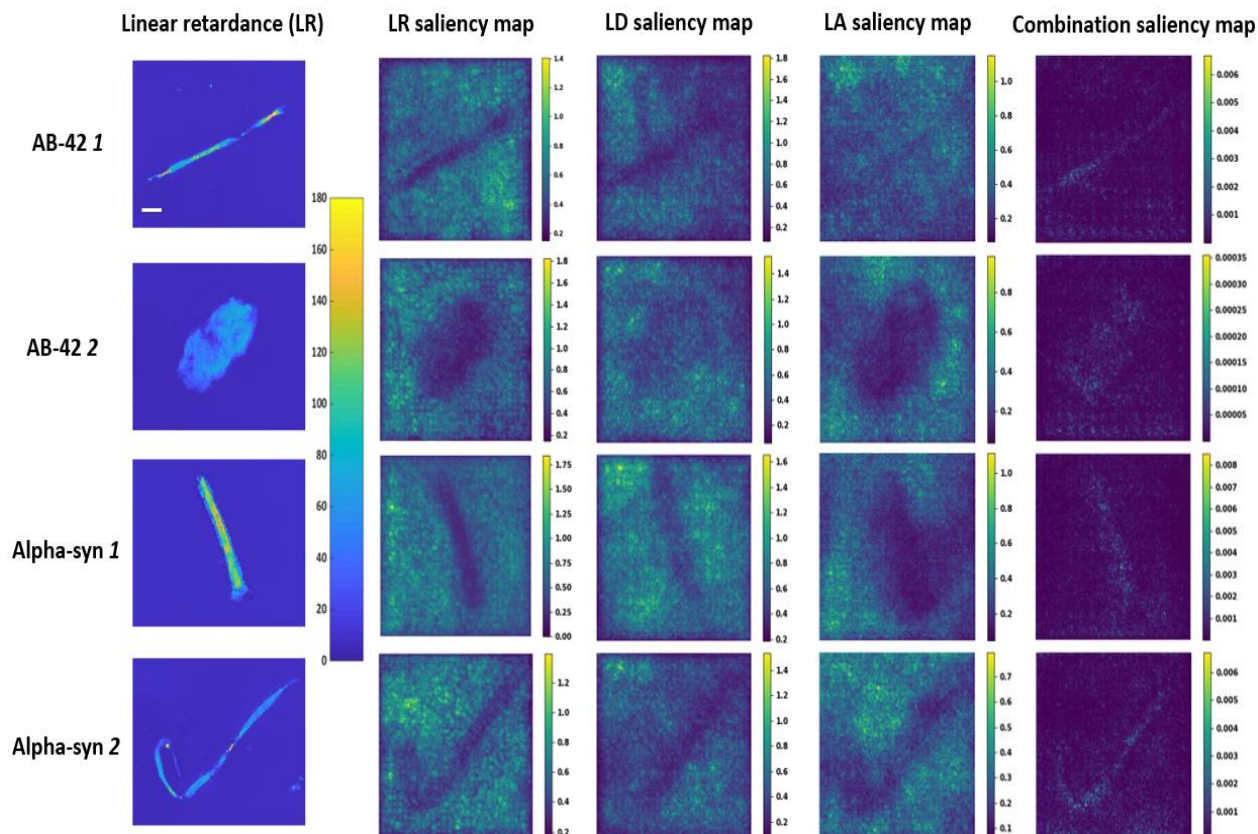
Figure 3.5. LR images and saliency maps of four pure protein deposits (the first two are Aβ-42 and the other two are alpha-syn). LR images are in the leftmost panel, then from left to right: Saliency map from the CNNs with LR, LD, LA and their combination image. Range of LR: [0°, 180°], LA: [0, 1], LD: [0, 1], combination: normalized to [0, 1]. Scale bar in the upper left panel: 20 μ.

The shapes of the four sample proteins can be clearly visualized in the saliency maps of LR, although the protein regions have lower rather than higher scores. The regions with lower saliency were in the same location as the original protein deposits with similar shapes.

The shapes of the protein deposits were less defined in some LD saliency maps compared to the LR saliency maps. In LD, the difference between the protein region and the background was less pronounced in Aβ-42, deposit *2*. In Aβ-42 deposit *1* and alpha-syn deposit *2*, some parts of the

46

background regions in the upper right corner shared the same saliency with the protein deposits. However, they still have roughly the same morphology as the corresponding protein deposits in the LR images.

The visualization of proteins in some LA saliency maps is closer to that in the LR images and saliency maps, but not in all. Overall the LR saliency maps best correlate with the corresponding deposit polarimetric images.

Unlike the saliency maps from individual properties, the saliency maps for the combination images showed higher values for the protein regions than for the background. The regions with high saliency are similar in shape to the corresponding LR images of the deposits. However, there were also regular bright spots in these saliency maps outside the deposit regions, especially in the lower parts of Aβ-42 *1* and *2*.

In conclusion, the above results on saliency are reassuring as they indicate that our CNN models are making decisions based on a part of the image known to be related to the shapes of the corresponding protein deposits, rather than randomly selected areas.
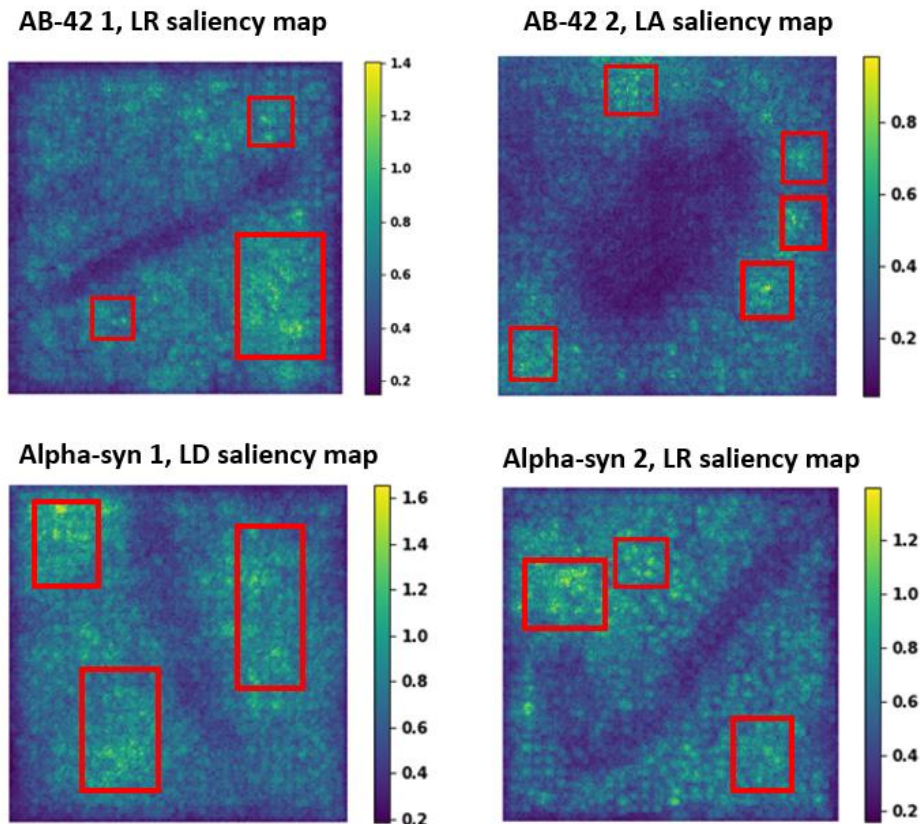
Figure 3.6. Four examples of saliency maps with non-uniformly highlighted backgrounds. The red boxes select some regions that are significantly brighter than the most background regions.

Although the shape of the protein deposits can be visualized in saliency maps, variations can be observed in the saliency values of the background regions. Taking the four protein deposits in Fig 3.6 as an example, the region selected by the red boxes are brighter than other regions in the backgrounds. In order to confirm whether this is caused by the presence of a birefringent protein deposit in the background, we examined the protein deposits under 45° PSG and 45° PSA. If the linear retardance signal were real, a signal should be found in the corresponding positions in the 45° PSG, 45° PSA microscope images, Fig 3.7 displays the microscope images of the four proteins in 45° PSG, 45° PSA setting.

Figure 3.7. The microscope images of the four example protein deposits under 45° PSG and 45° PSA, [0, 1].

In Fig 3.7 and in the original LR images, no signals could be found in the background thus we can exclude that those brighter regions are caused by the small background protein deposits.

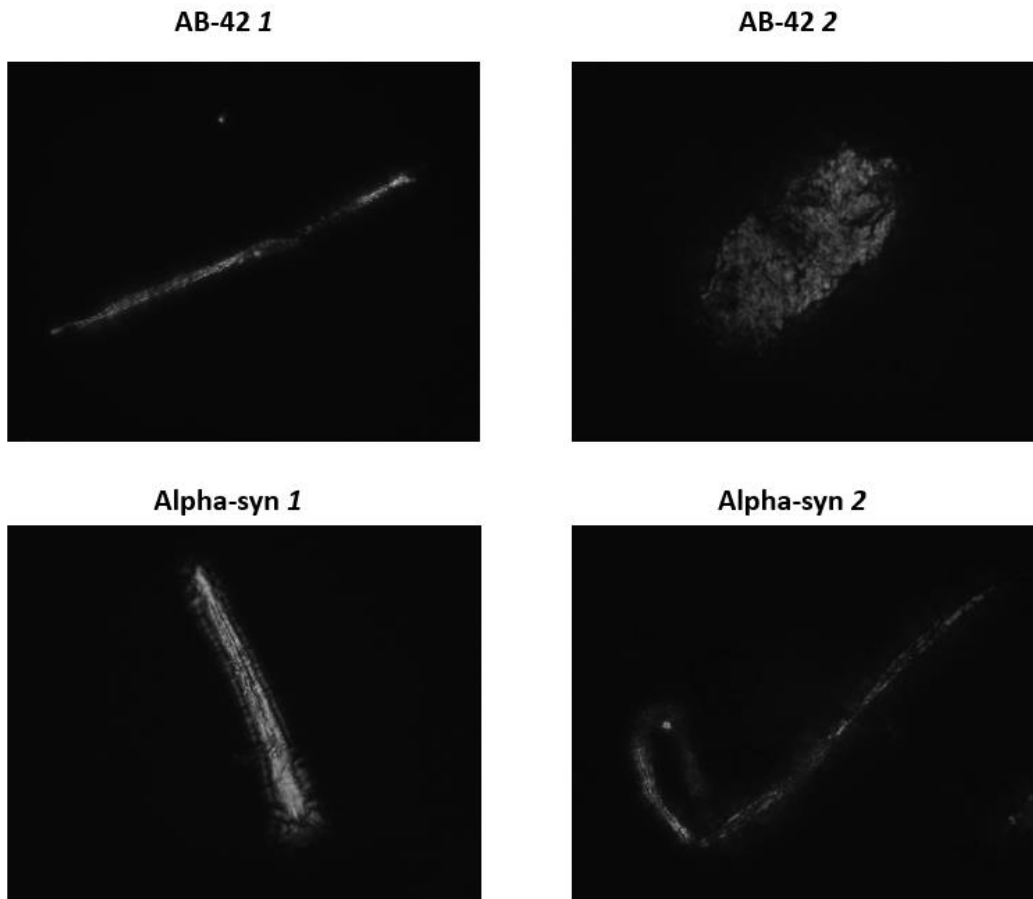For future direction, this project could potentially be further developed to differentiate four types of proteins: Aβ-38, Aβ-40, Aβ-42 and alpha-syn simultaneously. A decrease of Aβ-38 in the brain is associated with Frontotemporal lobar degeneration (FTLD)[77], which is also associated with alpha-syn[78]. Both Aβ-40 and Aβ-42 are associated with cerebral amyloid angiopathy (CAA) and AD, with Aβ-40 more prevalent in CAA and Aβ-42 prevalent in AD[79]. Thus, differentiating these four protein types could help distinguish between neurodegenerative diseases such as AD, PD, FTLD and CAA. Currently we are only classifying the polarimetry images of a deposits as containing different types of proteins. The method could be also be extended from protein classification to deposit detection. This would involve a pixel-by-pixel classification of the images to automatically localize the protein deposits, by using more advanced deep learning approaches such as YOLO[80] and R-CNN[81]. Such models could then be tested to determine the type and location of the detected protein deposits in *in-vivo* live eye imaging, as well as achieving a real-time image segmentation of the deposits.

The methods described in this project can differentiate pure Aβ-42 and alpha-syn deposits with a high accuracy of 90%, by using a modified convolutional neural network – Resnet 101 trained by LR images, without using dyes or immunohistochemistry. Using the method described in chapter 3, we expect that, using polarimetry, the thioflavin positive retinal amyloid deposits could first be identified with high accuracy in live-eye imaging. Subsequently, work in this chapter demonstrates that retinal deposits containing Aβ-42 could be distinguished from those containing alpha-syn by their polarimetric images. In turn, we have shown that the number of retinal deposits containing Aβ are predictive of the severity of Aβ in the brain, associated with AD. If it can be shown that alpha-syn in the retina is also predictive of alpha-syn in the brain, the differentiation of the two biomarkers in the retina may provide biomarkers for the differentiation of the neurodegenerative diseases associated with Aβ, for example AD from diseases associated with alpha-syn such as PD. The presented method may be applied in the future to the differentiation of additional neurodegenerative diseases, based on their interactions with polarized light. Compared to the other invasive methods, polarimetry is a promising dye-free

method of detecting retinal amyloid and other proteins in live eye imaging. The results reported here serve as an important first validation of the feasibility of this approach.

3.4 Discussion

In this study, pure deposits of Aβ-42 and alpha-syn were differentiated based on images of their polarimetric properties which map their interactions with polarized light. These properties in turn are calculated from 16 raw images taken in a polarimeter. Of the polarimetric properties tested, maps of linear retardance gave the best accuracy (above 90%) in differentiation and adding additional properties did not improve the accuracy. From the resulting saliency maps, the differences detected for classification of the two deposit types, were based on differences between the linear retardance of the deposits and the background.

Aβ-42 is known to form deposits of a well ordered fibrillar form. Although these deposits were known to interact with polarized light after a dye, Congo red aligned with the fibrils[5,52], our group was the first to show evidence that amyloid beta deposits have intrinsic interactions with polarized light in the absence of a dye[6]. Here we show analogous results for deposits of alpha-syn. Likely thus is also due to their fibrillar nature[82].

The differences between linear retardance maps of the two types of pure protein deposits which allowed CNN to classify them with such high accuracy could originate from several sources. Linear retardance at a given position is the product of thickness and birefringence. A subset of the pure Aβ-42 and alpha-syn deposits studied here were not significantly different in average thickness. All deposits were also not significantly different in their average linear retardance. This would suggest that the average birefringence of the two types of deposit may not differ significantly. Also, there were no statistically significant differences in size and shape-related metrics, measured using blob analysis. However, the maps of linear birefringence apparently do differ both in their fractal dimension and potentially the distribution of linear retardance values across the images. This may point to a difference in the way in which the two types of deposits grow and/or the exact arrangement of the fibrils within the deposits.

This work was done using a pretrained residual Convolutional Neural network with a number of different settings, of which the CNN model trained by LR with dropout in fully connected layers and the step-decay learning rate gave the best accuracy. Other CNN models trained by LA, LD and a combination image of LR, LD and LA gave lower accuracies than the CNN trained by LR.

There are limitations in this study. First, there are limited number of pure protein deposits for training CNN as it requires a considerable time to grow them. Only 360 protein deposits were used in this project, of which 70% (252) were used for training the networks. The lack of training data could cause overfitting and poor generalization of the models, which may be the reason why the training accuracies of the four CNNs all achieved 100%, but their testing accuracies did not. However, the overall accuracies achieved were high. The dropout technique was applied here to prevent overfitting. I tested other techniques such as L1 regularization and L2 regularization[75] have been tested but they were not as good as dropout. Collecting more data would still be the most effective way to improve the performance of CNN. Using only 10% of the protein deposits (36) for validation lead to validation learning curves that increased overall but had many oscillations. This leaves more samples for training and results in a high overall accuracy.

Second, the similarity between pure protein deposits and those in the retina containing these proteins needs to be examined. Similar variations in polarimetric properties across deposits have been found between retinal amyloid and pure Aβ-42 deposits (Corapi F, *et al*. IOVS 2018;59:ARVO E-Abstract 1582). The interactions with polarized light of pure alpha-syn deposits still need to be compared with interaction of protein deposits in the retinas of those with diseases associated with deposits containing alpha-syn for example Parkinson's disease. However, these initial results suggest that polarimetry may be an important label free method of detecting different protein deposits in the retina as biomarkers of different neurodegenerative diseases.

In section 3.3, the saliency maps of the CNNs trained by LR, LD and LA images showed de-emphasized rather than highlighted protein regions, with the shape of the deposits. This can be interpreted as another representation of protein deposits' shapes from the networks' perspective, accomplished by recognizing the shape of the regions around the protein deposits. This reinforces that, in differentiating the deposits of amyloid-β42 and α-synuclein, the CNN method is using the properties of the deposits and the surrounding regions.

We (M.C.W. Campbell, *et al.* IOVS 2010;51:ARVO E-Abstract 5778) and others[23,26] have demonstrated the presence of amyloid deposits in the retina in those with Alzheimer's disease, including the presence of Aβ-42. Alpha-syn deposits have been reported in the retinas of those with neurodegenerative diseases in which alpha-syn deposits are found in the brain. However, as discussed above, the polarimetric properties of LR, LA and LD of retinal deposits containing alpha-syn still need to be compared with those of pure alpha-syn deposits. Then the performance of our machine learning models in differentiating retinal deposits containing amyloid-β and those containing α-syn needs to be tested. Once the ability to differentiate the two deposit types were established, it could form the basis of a differential diagnosis of the two classes of neurodegenerative diseases which involve the two proteins, with the potential for earlier, less expensive diagnosis than the brain scans currently used[83].

Chapter 4

4 Conclusion

In this thesis, two different but associated research projects were presented on the theme of detecting amyloid deposits noninvasively in the retina of the eye. In Chapter 2, our group have shown that retinal deposits can be imaged by the Mueller matrix polarimetry with high resolution. By using the fluorescence microscope, we confirmed that most retinal deposits, detected in polarimetry, have thioflavin fluorescence signals, which is an established marker for amyloid.

However, a small percent of the retinal deposits are negative in fluorescence. Since imaging by fluorescence involves staining which is invasive for live eye imaging, machine learning algorithms were used to predict the presence of fluorescence signals of the detected deposits from their interactions with polarized light, without the use of dye. Of the machine learning methods used, the Random Forrest algorithm achieved the highest accuracy of 95%, thereby separating the presumed amyloid deposits from other retinal deposits.

Another protein, alpha-synuclein (alpha-syn) contains amyloid-like fibrils and also stains with thioflavin[58]. Since alpha-syn is related to other neurodegenerative diseases, including Parkinson's disease (PD)[59] which is also associated with alpha-syn in the retina[84], it is important to differentiate it from amyloid beta (Aβ) to allow the amyloid retinal deposits detected by polarimetry to be classified as either amyloid beta, as a biomarker of AD and related diseases or alpha-syn as a biomarker of PD and related diseases. For this purpose, in Chapter 3, Convolutional neural networks (CNNs), which can directly take the images of polarimetric properties as input, were trained and tested on images of selected properties of pure Aβ and alpha-syn protein deposits grown by others in our lab. The aim was to provide a real-time differentiation of retinal deposits containing Aβ and alpha-syn that could be applied to live eye imaging. Our best CNN model can achieve 90% accuracy. Thus it is promising to the

differentiate of retinal deposits containing Aβ from those containing alpha-syn using a noninvasive method, advantageous for live eye imaging and important to the differentiation of diseases associated with the two protein types.

For future directions, the work presented in this thesis can be further explored in several ways:

1. The machine learning classifiers in chapter 2 could be tested and optimized in *in vivo* studies in a larger sample size.
2. Improvements can be explored for the CNN models: including 1) increasing the numbers of images used as input through additional attempts at data augmentation (e.g. Random rotation, reflection and translation of the images). This would provide more training data without the collection of new data. 2) The filters and the feature maps of the convolutional layers could be visualized to increase the interpretability of neural networks and the impact of the size of the network on the accuracy of the protein prediction could also be explored.
3. The classification of protein deposits in the retina is a path to the differentiation of different neurodegenerative diseases. The CNN models can be developed to recognize four pure protein deposits: Aβ-42, Aβ-40, Aβ-38 and α-syn, the number of which are associated with AD, CAA, FTID and PD. Although the protein deposits interact with disease pathologies in a complex manner, being able to distinguish these deposit biomarkers is still beneficial to the research of diseases differentiation. The models would first be tested on pure protein deposits and then on retinal protein deposits.
4. The classification of proteins' types can also be a path to the object detection of the deposits' regions in live eye imaging using techniques like R-CNN/YOLO. By do this, researchers can not only know the type of a protein deposits, but also quick locating or even segmenting the deposits.

In conclusion, with the help of machine learning algorithms and deep neural network techniques, the existence of thioflavin fluorescence of a retinal deposit can be predicted from its interaction with polarized light. In addition, the AD biomarker Aβ-42 can also be differentiated from the PD biomarker alpha-syn by their polarization images. They together validate that the Mueller matrix polarimetry is a promising non-invasive dye-free method for detecting retinal amyloid and making the early diagnosis of AD.

Reference

1.   Alzherimer's association. Alzheimer's Facts and Figures Report.
        https://www.alz.org/alzheimers-dementia/facts-figures. Accessed June 20, 2020.

2.   Koronyo-Hamaoui M, Koronyo Y, Ljubimov A V., et al. Identification of amyloid
        plaques in retinas from Alzheimer's patients and noninvasive in vivo optical imaging of
        retinal plaques in a mouse model. *Neuroimage*. 2011;54:S204-S217.
        doi:10.1016/j.neuroimage.2010.06.020

3.   Keppler JS, Conti PS. A Cost Analysis of Positron Emission Tomography. *Am J
        Roentgenol*. 2001;177(1):31-40. doi:10.2214/ajr.177.1.1770031

4.   Campbell MCW. Method and system for imaging amyloid beta in the retina of the eye in
        association with alzheimer's disease. May 2011.

5.   Howie AJ, Brewer DB. Optical properties of amyloid stained by Congo red: History and
        mechanisms. *Micron*. 2009. doi:10.1016/j.micron.2008.10.002

6.   Campbell MCW, DeVries D, Emptage L, et al. Polarization properties of amyloid beta in
        the retina of the eye as a biomarker of Alzheimer's disease. In: *Bio-Optics: Design and
        Application, BODA 2015*. Optical Society of America (OSA); 2015:BM3A.4.
        doi:10.1364/boda.2015.bm3a.4

7.   Lu S, Chipman RA. Interpretation of Mueller matrices based on polar decomposition
        RETARDANCE : A REVIEW. 1996;13(5):1106-1113.

8.   World Health Organization., Alzheimer's Disease International. *Dementia : A Public
        Health Priority*. World Health Organization; 2012.

9.   McCulloch WS, Pitts W. A logical calculus of the ideas immanent in nervous activity.
        Bull Math Biophys. 1943;5(4):115-133. doi:10.1007/BF02478259

10.   Nair V, Hinton GE. *Rectified Linear Units Improve Restricted Boltzmann Machines*.

11.   Svozil D, Kvasnička V, Pospíchal J. Introduction to multi-layer feed-forward neural
        networks. In: *Chemometrics and Intelligent Laboratory Systems*. Vol 39. Elsevier;
        1997:43-62. doi:10.1016/S0169-7439(97)00061-0

12. Rumelhart DE, Hinton GE, Williams RJ. Learning representations by back-propagating errors. *Nature*. 1986;323(6088):533-536. doi:10.1038/323533a0

13. Goodfellow L, Yoshua B, Aaron C. *Deep Learning*. Cambridge: MIT press; 2016.

14. Hubel DH. Single unit activity in striate cortex of unrestrained cats. *J Physiol*. 1959;147(2):226-238. doi:10.1113/jphysiol.1959.sp006238

15. Hubel DH, Wiesel TN. *RECEPTIVE FIELDS OF SINGLE NEURONES IN THE CAT'S STRIATE CORTEX*. Vol 48.; 1959.

16. LeCun Y, Bottou L, Bengio Y, Haffner P. Gradient-based learning applied to document recognition. *Proc IEEE*. 1998;86(11):2278-2323. doi:10.1109/5.726791

17. Dumoulin V, Visin F, Box GEP. *A Guide to Convolution Arithmetic for Deep Learning*.; 2018. http://ethanschoonover.com/solarized. Accessed May 25, 2020.

18. Qiu Y, Campbell MCW, Jin T, Mason E. Predicting Thioflavin Fluorescence of Retinal Amyloid Deposits Associated With Alzheimer ' s Disease by Their Polarimetric Properties. *Trans Vis Sci Tech*. 2020. https://doi.org/10.1167/tvst.0.0.1996.

19. Hyman BT, Phelps CH, Beach TG, et al. National Institute on Aging–Alzheimer's Association guidelines for the neuropathologic assessment of Alzheimer's disease. *Alzheimer's Dement*. 2012;8(1):1-13. doi:10.1016/J.JALZ.2011.10.007

20. Jack CR, Bennett DA, Blennow K, et al. NIA-AA Research Framework: Toward a biological definition of Alzheimer's disease. *Alzheimer's Dement*. 2018;14(4):535-562. doi:10.1016/j.jalz.2018.02.018

21. Klunk WE, Engler H, Nordberg A, et al. Imaging Brain Amyloid in Alzheimer's Disease with Pittsburgh Compound-B. *Ann Neurol*. 2004;55(3):306-319. doi:10.1002/ana.20009

22. Anoop A, Singh PK, Jacob RS, Maji SK. CSF Biomarkers for Alzheimer's Disease Diagnosis. *Int J Alzheimers Dis*. 2010;2010(Table 1):1-12. doi:10.4061/2010/606802

23. Ising C, Stanley M, Holtzman D. Current thinking on the mechanistic basis of Alzheimer's and implications for drug development. *Clin Pharmacol Ther*. 2015;98(5):469-471. doi:10.1002/cpt.200

24. Sabbagh MN, Blennow K. Peripheral Biomarkers for Alzheimer's Disease: Update and Progress. *Neurol Ther*. 2019;8:33-36. doi:10.1007/s40120-019-00171-6

25. Lim JKH, Li QX, He Z, et al. The eye as a biomarker for Alzheimer's disease. *Front Neurosci*. 2016;10(NOV). doi:10.3389/fnins.2016.00536

26. Begum A, Kvanta A, Seregard S, et al. Retinal amyloid pathology and proof-of-concept imaging trial in Alzheimer's disease. *J Pharmacol Exp Ther*. 2017;326(1):196-208. doi:10.1172/JCI.INSIGHT.93621

27. Hart NJ, Koronyo Y, Black KL, Koronyo-Hamaoui M. Ocular indicators of Alzheimer's: exploring disease in the retina. *Acta Neuropathol*. 2016;132(6):767-787. doi:10.1007/s00401-016-1613-6

28. den Haan J, Morrema THJ, Verbraak FD, et al. Amyloid-beta and phosphorylated tau in post-mortem Alzheimer's disease retinas. *Acta Neuropathol Commun*. 2018;6(1):147. doi:10.1186/s40478-018-0650-x

29. Westermark G., Johnson K., Westermark P. Staining methods for identification of amyloid in tissue. *Methods Enzymol*. 1999;309:3-25.

30. Koronyo Y, Biggs D, Barron E, et al. Retinal amyloid pathology and proof-of-concept imaging trial in Alzheimer's disease. *JCI insight*. 2017;2(16). doi:10.1172/jci.insight.93621

31. Campbell MCW, Emptage L, Redekop R, et al. AMYLOID DEPOSITS IMAGED IN POSTMORTEM RETINAS USING POLARIMETRY PREDICT THE SEVERITY OF A POSTMORTEM BRAIN BASED DIAGNOSIS OF ALZHEIMER'S DISEASE. *Alzheimer's Dement*. 2018;14(7):P774-P775. doi:10.1016/j.jalz.2018.06.947

32. Wördehoff MM, Hoyer W. α-Synuclein Aggregation Monitored by Thioflavin T Fluorescence Assay. *Bio-protocol*. 2018;8(14). doi:10.21769/BioProtoc.2941

33. Eberling JL, Dave KD, Frasier MA. α-synuclein imaging: A critical need for parkinson's disease research. *J Parkinsons Dis*. 2013;3(4):565-567. doi:10.3233/JPD-130247

34. Kepe V, Moghbel MC, Långströmd B, et al. Amyloid-β positron emission tomography

imaging probes: A critical review. *J Alzheimer's Dis*. 2013;36(4):613-631. doi:10.3233/JAD-130485

35.   Magnin B, Mesrob L, Kinkingnéhun S, et al. Support vector machine-based classification of Alzheimer's disease from whole-brain anatomical MRI. *Neuroradiology*. 2009;51(2):73-83. doi:10.1007/s00234-008-0463-x

36.   Zhang Y, Dong Z, Phillips P, et al. Detection of subjects and brain regions related to Alzheimer's disease using 3D MRI scans based on eigenbrain and machine learning. *Front Comput Neurosci*. 2015;9(JUNE):1-15. doi:10.3389/fncom.2015.0006

37.   Lebedev A V., Westman E, Van Westen GJP, et al. Random Forest ensembles for detection and prediction of Alzheimer's disease with a good between-cohort robustness. *NeuroImage Clin*. 2014;6:115-125. doi:10.1016/j.nicl.2014.08.023

38.   Fuller AR, Zawadzki RJ, Choi S, Wiley DF, Werner JS, Hamann B. Segmentation of three-dimensional retinal image data. *IEEE Trans Vis Comput Graph*. 2007;13(6):1719-1726. doi:10.1109/TVCG.2007.70590

39.   Li X, Liao R, Zhou J, Leung PTY, Yan M, Ma H. Classification of morphologically similar algae and cyanobacteria using Mueller matrix imaging and convolutional neural networks. *Appl Opt*. 2017;56(23):6520. doi:10.1364/ao.56.006520

40.   Michael B, Casimer D, Jay E, et al. *Handbook of Optics*. Third edit. New York: The McGraw-Hill Companies, Inc; 2009.

41.   Arteaga O, Garcia-Caurel E, Ossikovski R. Anisotropy coefficients of a Mueller matrix. *J Opt Soc Am A*. 2011;28(4):548. doi:10.1364/josaa.28.000548

42.   Sun M, He H, Zeng N, et al. Characterizing the microstructures of biological tissues using Mueller matrix and transformed polarization parameters. 2014;5(12):329-340. doi:10.1364/BOE.5.004223

43.   Zeng N. A possible quantitative Mueller matrix transformation technique for anisotropic scattering media / Eine mögliche ... A possible quantitative Mueller matrix transformation technique for anisotropic scattering media. 2013;(February). doi:10.1515/plm-2012-0052

59

44. Espinosa-Luna R, Bernabeu E. On the Q(M) depolarization metric. *Opt Commun*. 2007;277(2):256-258. doi:10.1016/j.optcom.2007.05.051

45. Rahman MM, Davis DN. Addressing the Class Imbalance Problem in Medical Datasets. 2013;3(2). doi:10.7763/IJMLC.2013.V3.307

46. Han H, Wang W, Mao B. Borderline-SMOTE : A New Over-Sampling Method in. 2005:878-887.

47. Chawla N V, Bowyer KW, Hall LO. SMOTE : Synthetic Minority Over-sampling Technique. 2002;16:321-357.

48. Stone M. Cross-Validatory Choice and Assessment of Statistical Predictions (With Discussion). *J R Stat Soc Ser B*. 1976;38(1):102-102. doi:10.1111/j.2517-6161.1976.tb01573.x

49. Pedregosa F, Varoquaux G, Gramfort A, Michel V, Thirion B. Scikit-learn: Machine Learning in Python. *J Mach Learn Res*. 2011;12:2825--2830.

50. Bradley AP. The use of the area under the ROC curve in the evaluation of machine learning algorithms. *Pattern Recognit*. 1997;30(7):1145-1159. doi:10.1016/S0031-3203(96)00142-2

51. Menze BH, Kelm BM, Masuch R, et al. A comparison of random forest and its Gini importance with standard chemometric methods for the feature selection and classification of spectral data. 2009;16:1-16. doi:10.1186/1471-2105-10-213

52. Yakupova EI, Bobyleva LG, Vikhlyantsev IM, Bobylev AG. Congo Red and amyloids: History and relationship. *Biosci Rep*. 2019;39(1). doi:10.1042/BSR20181415

53. Krebs MRH, Bromley EHC, Donald AM. The binding of thioflavin-T to amyloid fibrils: localisation and implications. *J Struct Biol*. 2005;149(1):30-37. doi:10.1016/J.JSB.2004.08.002

54. Atwood CS, Martins RN, Smith MA, Perry G. Senile plaque composition and posttranslational modification of amyloid-β peptide and associated proteins. *Peptides*. 2002;23(7):1343-1350. doi:10.1016/S0196-9781(02)00070-0

55. José J GP, Razvigor O. *Polarized Light and the Mueller Matrix Approach*. Boca Raton: CRC Press; 2016.

56. Van Der Maaten L, Hinton G. *Visualizing Data Using T-SNE*. Vol 9.; 2008.

57. Campbell MCW. Method and system for imaging amyloid beta in the retina of the eye in association with Alzheimer's disease. 2015.

58. El-Agnaf OMA, Irvine GB. Review: Formation and properties of amyloid-like fibrils derived from α-synuclein and related proteins. *J Struct Biol*. 2000;130(2-3):300-309. doi:10.1006/jsbi.2000.4262

59. Marsh SE, Blurton-Jones M. Examining the mechanisms that link β-amyloid and α-synuclein pathologies. *Alzheimer's Res Ther*. 2012;4(2):1-8. doi:10.1186/alzrt109

60. Raghavan R, Khin-nu C, Brown A, et al. Detection of Lewy Bodies in Trisomy 21 (Down's Syndrome). *Can J Neurol Sci / J Can des Sci Neurol*. 1993;20(1):48-51. doi:10.1017/S0317167100047405

61. Hamilton RL. Lewy Bodies in Alzheimer's Disease: A Neuropathological Review of 145 Cases Using α-Synuclein Immunohistochemistry. *Brain Pathol*. 2000;10(3):378-384. doi:10.1111/j.1750-3639.2000.tb00269.x

62. Trojanowski JQ, Lieberburg I, Lemere C, et al. Emerging Alzheimer's disease therapies: Focusing on the future. In: *Neurobiology of Aging*. Vol 23. Neurobiol Aging; 2002:985-990. doi:10.1016/S0197-4580(02)00123-9

63. Corbillé A-G, Letournel F, Kordower JH, et al. Evaluation of alpha-synuclein immunohistochemical methods for the detection of Lewy-type synucleinopathy in gastrointestinal biopsies. *Acta Neuropathol Commun*. 2016;4(1):35. doi:10.1186/s40478-016-0305-8

64. Deng J, Dong W, Socher R, Li L-J, Kai Li, Li Fei-Fei. ImageNet: A large-scale hierarchical image database. In: Institute of Electrical and Electronics Engineers (IEEE); 2009:248-255. doi:10.1109/cvpr.2009.5206848

65. Schmidt-Erfurth U, Sadeghipour A, Gerendas BS, Waldstein SM, Bogunović H. Artificial

intelligence in retina. *Prog Retin Eye Res*. 2018;67:1-29. doi:10.1016/j.preteyeres.2018.07.004

66. Chen X, Xu Y, Kee Wong DW, Wong TY, Liu J. Glaucoma detection based on deep convolutional neural network. In: *Proceedings of the Annual International Conference of the IEEE Engineering in Medicine and Biology Society, EMBS*. Vol 2015-November. Institute of Electrical and Electronics Engineers Inc.; 2015:715-718. doi:10.1109/EMBC.2015.7318462

67. Oh SL, Hagiwara Y, Raghavendra U, et al. A deep learning approach for Parkinson's disease diagnosis from EEG signals. *Neural Comput Appl*. 2018;5. doi:10.1007/s00521-018-3689-5

68. He K, Zhang X, Ren S, Sun J. Deep residual learning for image recognition. *Proc IEEE Comput Soc Conf Comput Vis Pattern Recognit*. 2016;2016-Decem:770-778. doi:10.1109/CVPR.2016.90

69. Lu W, Tong Y, Yu Y, Xing Y, Chen C, Shen Y. Deep learning-based automated classification of multi-categorical abnormalities from optical coherence tomography images. *Transl Vis Sci Technol*. 2018;7(6):0-9. doi:10.1167/tvst.7.6.41

70. Narin A, Kaya C, Pamuk Z. Automatic Detection of Coronavirus Disease (COVID-19) Using X-ray Images and Deep Convolutional Neural Networks. March 2020. http://arxiv.org/abs/2003.10849. Accessed June 4, 2020.

71. Simonyan K, Zisserman A. *VERY DEEP CONVOLUTIONAL NETWORKS FOR LARGE-SCALE IMAGE RECOGNITION*.; 2015. http://www.robots.ox.ac.uk/. Accessed May 29, 2020.

72. Srivastava N, Hinton G, Krizhevsky A, Salakhutdinov R. *Dropout: A Simple Way to Prevent Neural Networks from Overfitting*. Vol 15.; 2014.

73. Wylie CR, Barrett LC, Wylie CR. *Advanced Engineering Mathematics*. 4th ed.; 1960.

74. LeCun YA, Bottou L, Orr GB, Müller K-R. Efficient BackProp. In: Springer, Berlin, Heidelberg; 2012:9-48. doi:10.1007/978-3-642-35289-8_3

75.   Kim P. *MATLAB Deep Learning*.; 2017. doi:10.1007/978-1-4842-2845-6

76.   Simonyan K, Vedaldi A, Zisserman A. Deep inside convolutional networks: Visualising image classification models and saliency maps. *2nd Int Conf Learn Represent ICLR 2014 - Work Track Proc*. 2014:1-8.

77.   Kummer MP, Heneka MT. Truncated and modified amyloid-beta species. *Alzheimer's Res Ther*. 2014;6(3):1-9. doi:10.1186/alzrt258

78.   Aoki N, Boyer PJ, Lund C, et al. Atypical multiple system atrophy is a new subtype of frontotemporal lobar degeneration: frontotemporal lobar degeneration associated with α-synuclein. *Acta Neuropathol*. 2015;130(1):93-105. doi:10.1007/s00401-015-1442-z

79.   Gkanatsiou E, Portelius E, Toomey CE, et al. A distinct brain beta amyloid signature in cerebral amyloid angiopathy compared to Alzheimer's disease. *Neurosci Lett*. 2019;701:125-131. doi:10.1016/j.neulet.2019.02.033

80.   Redmon J, Divvala S, Girshick R, Farhadi A. You Only Look Once: Unified, Real-Time Object Detection. *Cvpr*. June 2015. http://arxiv.org/abs/1506.02640. Accessed June 14, 2020.

81.   Girshick R, Donahue J, Darrell T, Malik J. *Rich Feature Hierarchies for Accurate Object Detection and Semantic Segmentation*. http://arxiv. Accessed June 14, 2020.

82.   Conway KA, Harper JD, Lansbury PT. Accelerated in vitro fibril formation by a mutant α-synuclein linked to early-onset Parkinson disease. *Nat Med*. 1998;4(11):1318-1320. doi:10.1038/3311

83.   Mathis CA, Lopresti BJ, Ikonomovic MD, Klunk WE. Small-molecule PET Tracers for Imaging Proteinopathies. *Semin Nucl Med*. 2017;47(5):553-575. doi:10.1053/j.semnuclmed.2017.06.003

84.   Veys L, Vandenabeele M, Ortuño-Lizarán I, et al. Retinal α-synuclein deposits in Parkinson's disease patients and animal models. *Acta Neuropathol*. 2019;137(3):379-395. doi:10.1007/s00401-018-01956-z

Appendix 1: Definitions of machine learning terms not defined in the text

Words and phrases in bold are used in the main text.

Feature: A **feature** is a property input to the **machine learning algorithm**. In this paper we use polarimetric properties which describe interactions of the sample with polarized light.

Datasets of each class: The groups into which the data is classified, each of which has a unique label, are referred to as **classes**. In our case, we have two datasets of deposits labelled with the **classes**, thioflavin positive and thioflavin negative, both members of which are described by polarimetric properties. When datasets contain unequal numbers of data, this is referred to as **data imbalance**.

Machine learning algorithm: Computer programs (algorithms) that can "learn" from **training data** and improve their performance in predicting the **class** of input **testing data**. Our two datasets are labelled thioflavin positive and thioflavin negative. After learning **training**, these programs are given **testing data**, which they classify into the **classes**. These algorithms are also known as **classifiers**. The algorithms we test are:

> **Linear discriminant analysis (LDA):** uses **training data** to learn linear equations which produce values which are close for members of the same **dataset**, and far apart for members of different **datasets**. These equations are then used to classify **testing data** into **classes**.

> **Supporting vector machine (SVM):** When **training, SVM** finds a decision boundary in the **feature** space to separate the different **datasets** as far as possible. **Testing data** are classified based on which side of the boundary they fall on. **SVM** heavily weights data close to the decision boundary.

> **Random forest (RF): RF** uses many decision trees to generate a consensus decision. A decision tree classifies data points by using multiple properties to differentiate data into separate **classes**. When **training**, many trees fit a random subset of the **training** set. Each data point is available to be sampled multiple times during training. This is called bootstrapping.

When testing, bootstrapping again generates many subsets, and each is classified. This classification uses a decision tree based on **Gini impurity**. Data points are then classified into the **class** where it was most frequently placed.

> **Gini impurity:** is a commonly used metric in **RF** decision trees to decide the optimal property to split the data into subsets. In general, as the splitting continues, the amount of data in branch nodes of a decision tree which belong to the same **class** should increase, this implies that the "purity" of the nodes is increasing. The purity of a **dataset** varies inversely with Gini impurity (Equation 3). The property with the smallest Gini impurity is chosen for node splitting. The decrease in Gini impurity at each node over the tree is summed to calculate **the variable importance of each property**.

Oversampling strategy: If the **datasets** of each **class** are not balanced in their number of data points, these methods can be applied to increase the data points in the dataset with lower numbers (**minority**, in our case thioflavin negative deposits). Our **majority dataset** consists of thioflavin positive deposits.

> **K-nearest neighbor analysis, used in oversampling:** Determine the k points nearest a given point (from the nearest to the kth nearest). The points are defined by the values of the mean and STD of each of the polarimetric properties. The nearest points have the most similar properties.

> **SMOTE algorithm:** A commonly used algorithm to generate synthetic samples (**oversample**) in the **minority dataset** to balance the number in the **majority dataset**. The algorithm begins by searching for the **k-nearest neighbors** of the same class (k is usually set to 5) for every sample in the **minority dataset**, then randomly generates a number of new synthetic data points along the line between the minority datapoint and its nearest neighbors. The number of synthetic data points matches the total number in the **minority dataset** to the **majority dataset**.

> **Borderline-SMOTE oversampling:** Based on SMOTE oversampling, **borderline-SMOTE** only performs the **SMOTE algorithm** on examples in the **minority dataset** that have nearest neighbors in the **majority dataset** as these are easily misclassified.

Cross-validation: (10-fold): divides the data into 10 subsets with similar size. One subset is used as the **testing data** and the other 9 are the **training data**. This is repeated for the other 9 subsets and the average of the 10 results is output.

t-distributed stochastic neighbor embedding (t-SNE)[56] test: a machine learning method for dimension reduction that can help to identify the patterns of properties in the **datasets**. The main advantage of t-SNE over other dimension reduction methods (such as principal component analysis) is the ability to maintain local patterns in the dataset. This means that similar points in high-dimensional space are still close to each other in a lower-dimensional projection.

> **Perplexity:** Perplexity is a parameter that controls the dimension reduction in **t-SNE**. It can be interpreted as the nearest neighbors considered when matching the original (high-dimensional space) and the fitted (low-dimensional space) of each point. A smaller perplexity means only a few points are considered as the nearest neighbors when doing fitting, which highlights the information local to the data points. A higher perplexity means that more points are considered as the nearest neighbors, giving a more "global view".

Convolutional Neural Network (CNN): is a type of deep neural network model which involves convolutional layers and convolution operations.

> **Batch normalization:** Batch normalization is usually applied after the fully connected layer or the convolutional layer of a CNN, to normalize the output of each neuron in the layer into a unit Gaussian distribution before being trained in the next layer. Since the network is usually trained by mini-batch, the normalization will be implemented on the data with a batch size and is thus called **batch normalization**.

> **Momentum:** is added when updating the weights, with the aim of adjusting the weights by considering the impact from the previous gradients. Thus, the weight ω will be updated to ω' by

$$\omega' = \omega - m$$

$$\text{where } m = \beta m^- + \eta \frac{\partial E_k}{\partial \omega}$$

> m is the momentum vector, m^- is the previous momentum vector, E_k is the difference between the predicted label and the label measured by the loss function, and β is a hyperparameter range from 0 to 1 for controlling the momentum. In this thesis, β is set to be

0.9. Compared to Eq 1.33 in Chapter 1, one can find the weight updated by momentum will take the previous gradients $\frac{\partial E_k^-}{\partial \omega^-}$ into consideration.

The score returned by the neural network: ranges from 0 to 1 with respect to each class, which describes the probability of the input belonging to each class, respectively. For example, if the score returned by CNN for a given input is (0.2, 0.8) with respect to Aβ-42 and alpha-syn, then it is more likely to be alpha-syn.

Dropout: is a popular regularization technique for deep neural networks. During the training, every neuron in each layer will have a certain probability to be temporarily inactive. Inactive means that the inactive neuron will not be connected with other neurons in the network, it is "dropped out". The probability of this is known as the dropout rate.

Learning curves: a plot that shows the improvement of training or validation in accuracy, with respect to the training/validation time.

Mini-batch: Instead of computing the SGD of all the data in a dataset simultaneously, in practice, the dataset is usually divided into multiple small batches, known as the **mini-batches** with a **batch size** equal to the number of samples included in each mini-batch. Then SGD is performed on each mini-batch in turn.

Epochs: When the neural network learns from all the training data in a training dataset, it is called an **epoch**. Normally, a neural network will need to be trained several times in order to get a decent performance and use several epochs of data.

L1 regularization: In order to alleviate the problem of overfitting, a penalty term is often added to the loss function. If the introduced penalty term is the L1 norm of the weights ω, then it is called **L1 regularization**.

C = The cross entropy loss + $\lambda\|\omega\|_1$, where $\lambda > 0$ and can be specified by users to control the regularization.

L2 regularization: Similar to **L1 regularization**, if the introduced penalty term is the L2 norm of the weights ω, then it is called **L2 regularization**.

$\mathbf{C} = $ The cross entropy loss $+ \ \lambda \|\omega\|_2^2$, where $\lambda > 0$ and can be specified by users to control the regularization.

Appendix 2

Table A 1. **Equations for the polarimetric properties used as features in the machine learning algorithms**.

M_{ij} is the Mueller matrix element in the ith row and jth column. M_Δ and M_R are the depolarization and retardance matrices obtained from polar decomposition[7]

Feature name	Equation
Linear retardance (LR)	$$\frac{\sqrt{(M_{R23} - M_{R32})^2 + (M_{R31} - M_{R13})^2}}{2sin\{cos^{-1}\left[\frac{tr(M_R)}{2} - 1\right]\}}$$
Circular retardance	$$\frac{M_{R12} - M_{R21}}{2sin\{cos^{-1}\left[\frac{tr(M_R)}{2} - 1\right]\}}$$
Linear diattenuation	$$\sqrt{(M_{01}{}^2 + M_{02}{}^2)}$$
Circular diattenuation	M_{03}
Depolarization power	$$1 - \frac{|tr(M_\Delta) - 1|}{3}$$
Metric b	$$\frac{M_{22} + M_{33}}{2}$$
Metric t	$$\frac{\sqrt{(M_{22} - M_{33})^2 + (M_{23} + M_{32})^2}}{2}$$
Metric A	$$\frac{2b * t}{b^2 + t^2}$$
Metric x	$$\frac{tan^{-1}(\frac{M_{31}}{M_{21}})}{2}$$
Linear polarizance	$$\sqrt{M_{10}{}^2 + M_{20}{}^2}$$
Circular polarizance	M_{30}

Q metric	$$\frac{\frac{\sum_{i,j=0}^{3}(M_{ij}{}^2 - M_{00}{}^2)}{M_{00}{}^2} - M_{01}{}^2 - M_{02}{}^2 - M_{03}{}^2}{1 + M_{01}{}^2 + M_{02}{}^2 + M_{03}{}^2}$$
Linear anisotropy (LA)	$$\frac{\sqrt{(M_{01} + M_{10})^2 + (M_{02} + M_{20})^2 + (M_{23} - M_{32})^2 + (M_{13} - M_{31})^2}}{\sqrt{\Sigma}}$$
Circular anisotropy	$$\frac{\sqrt{(M_{03} + M_{30})^2 + (M_{12} - M_{21})^2}}{\sqrt{\Sigma}}$$

where $\Sigma = \left(3M_{00}{}^2 - M_{11}{}^2 - M_{22}{}^2 - M_{33}{}^2\right) + 2(M_{01}M_{10} + M_{02}M_{20} + M_{03}M_{30} - M_{23}M_{32} - M_{13}M_{31} - M_{12}M_{21})$,.

Table A 2. **Hyper-parameters of SVM and RF**

where the parameters used are defined in[49]

Classifier	Hyper-parameter distributions
SVM	Kernel: [radial basis function, polynomial, sigmoid] Degree of polynomial kernel function: [1,2,3] Gamma: [0.001, 0.01, 0.1] Shrinking: [True, False] Cost parameter: 1 Search iteration:30
RF	Number of trees: a random integer in [100,1000] Bootstrap: [True, False] Max features of splitting: a random integer in [1,28] Minimal sample of splitting: a random integer in [2,27] Criterion: [Gini impurity, information gain] Maximum tree depth: unlimited Search iteration: 100
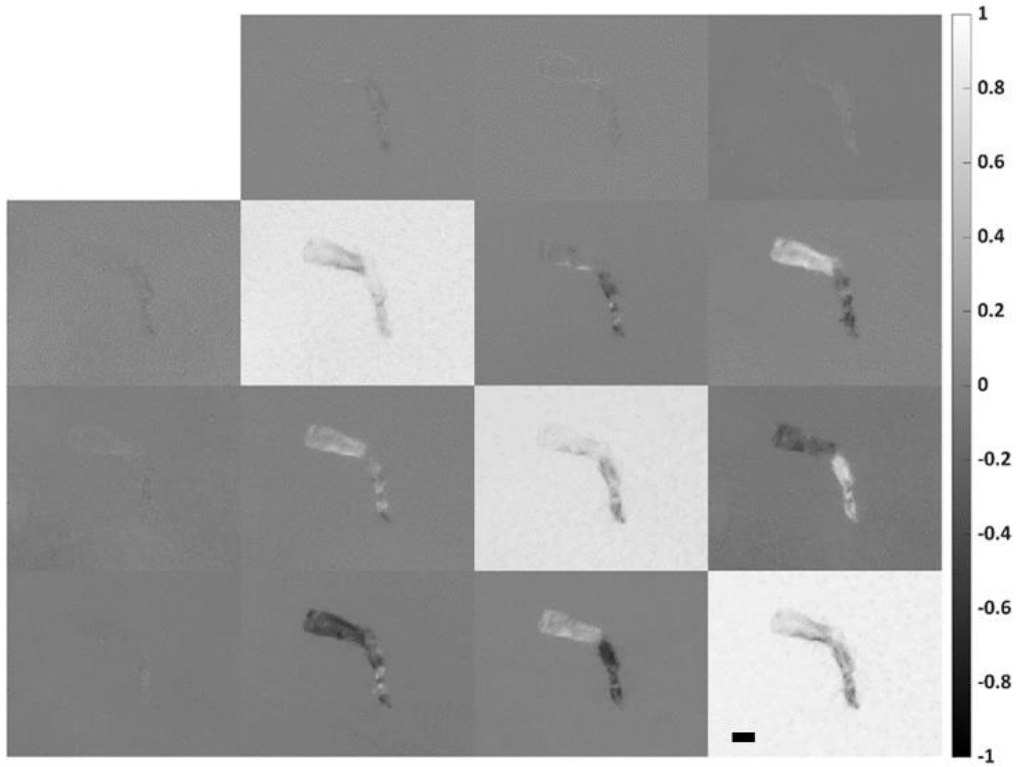
Figure A1. A spatially resolved Mueller matrix (MM) of a polarimetric and fluorescence positive deposit. Elements are coded by row and column number (M00 to M33) and each pixel position has 16 elements associated with it. The matrix elements are normalized by M00.

Appendix 3: Permission Statements

Francesco Visin <visin@google.com>
Today, 2:23 PM
Yunyi Qiu ⩔

↩ Reply all | ⌄

Dear Yunyi,

Thank you for your appreciation!
Feel free to use the images and animations of the guide with proper attribution.

Best of luck with your thesis!

Ciao,
Francesco

Francesco Visin | Research Scientist | DeepMind | visin@google.com
•••

Yunyi Qiu
Today, 12:54 PM

↩ | ⌄

Dear Dr. Francesco Visin,

I am a graduate student doing a research-based physics grad at the University of Waterloo. I am currently writing my graduate thesis which includes the introduction of the convolutional neural network. I found the convolution animations on your GitHub: https://github.com/vdumoulin/conv_arithmetic very nice and hope I can get you authorization to use them in my thesis (which won't be used in any commercial purpose).

I have referenced the paper you have published on arxiv:https://arxiv.org/abs/1603.07285. But as a requirement from University, I still need to have your permission in order to use the images.

I would be really appreciated it if I can have your authorization.

Best wishes
Yunyi Qiu

Figure A2. Permission for inclusion of figure 1.4 and 1.5.

Figure A3. Permission for inclusion of the paper on TVST journal as my second chapter, in which I am the first author.